Behaviour of S, SO and SO_3 on Pt (001), (011) and (111) surfaces: A DFT Study

Marietjie J. Ungerer,[1,2] Cornelia G.C.E. van Sittert *[1] and Nora H. de Leeuw *[2,3]

[1] Laboratory for Applied Molecular Modelling, Research Focus Area: Chemical Resource Beneficiation, North-West University, Private Bag X6001, Potchefstroom, 2520, South Africa

[2] School of Chemistry, Cardiff University, Main Building, Park Place, Cardiff CF10 3AT, United Kingdom

[3] School of Chemistry, Faculty of Engineering and Physical Sciences, University of Leeds, Leeds LS2 9JT, United Kingdom

*(CGCEvS) E-mail address: cornie.vansittert@nwu.ac.za

*(NHdL) E-mail address: n.h.deleeuw@leeds.ac.uk

Abstract

In the hybrid sulphur (HyS) cycle, the reaction between SO_2 and H_2O is manipulated to produce hydrogen, with water and sulphuric acid as by-products. However, sulphur poisoning of the catalyst has been widely reported to occur in this cycle, which is due to strong chemisorption of sulphur on the metal surface. The catalysts may deactivate as a result of these impurities present in the reactants or incorporated in the catalyst during its preparation and operation of the HyS cycle.

Here, we report a density functional theory (DFT) investigation of the interaction between S, SO and SO_3 with the Pt (001), (011) and (111) surfaces. First, we have investigated the adsorption of single gas phase molecules on the three Pt surfaces. During adsorption, the 4F hollow sites on the (001) and (011) surfaces and the *fcc* hollow site on the (111) surface were preferred. S adsorption followed the trend of $(001)_{4F}$ > $(011)_{4F}$ > $(111)_{fcc}$, while SO adsorption showed $(001)_{4F}$ > $(011)_{bridge/4F}$ > $(111)_{fcc}$ and SO_3 adsorption was most stable in a S,O,O bound configuration on the $(001)_{4F}$ > $(011)_{4F}$ > $(111)_{fcc}$ sites.

The surface coverage was increased on all the surfaces until a monolayer was obtained. The highest surface coverage for S shows the trend $(001)_S$ = $(111)_S$ > $(011)_S$, and for SO it is $(001)_{SO}$ > $(011)_{SO}$ > $(111)_{SO}$, similar to SO_3 where we found $(001)_{SO3}$ > $(011)_{SO3}$ > $(111)_{SO3}$. These trends indicate that the (001) surface is more susceptible to S species poisoning. It was also evident that both the (001) and (111) surfaces were reactive towards S, leading to the formation of S_2. High coverage of SO_3 showed the formation of SO_2 and SO_4, especially on the (011) surface. The thermodynamics indicated that an increased temperature up to 2000 K resulted in Pt surfaces fully covered with elemental S. The SO coverage showed $\theta \geq 1.00$ on both the (001) and (011) surfaces, and $\theta = 0.78$ for the (111) in the experimental region where the HyS cycle is operated. Lower coverages of SO_3 were observed due to the size of the molecule.

1. Introduction

The oxidation of sulphur dioxide (SO_2) in aqueous solutions has been studied for over a century [1–3]. With the advent of industrialisation, automation and massive population growth, the presence of SO_2 has increased not only as a by-product of industry, but also as a result of the uses of new technologies in everyday life [4,5]. It has been shown that atmospheric SO_2 has a detrimental effect, not only on the environment but also human life [5,6]. With more countries and governments enforcing limitations on industry to reduce SO_2 emissions [5–7], new technologies are emerging for either the capture [8] or re-utilisation of SO_2 [9,10].

One viable option for the utilisation of SO_2 is in the hybrid sulphur (HyS) cycle, where SO_2 reacts with water (H_2O) at temperatures between 80 and 120 ºC to form sulphuric acid (H_2SO_4) and hydrogen (H_2). The H_2SO_4 can be re-utilised by thermal decomposition (> 800 ºC) to form oxygen (O_2), H_2O and SO_2. The net reaction of this cycle is therefore the splitting of H_2O into O_2 and H_2. In turn, H_2 is considered a potentially viable solution to address sustainable energy production as it is an ideal energy carrier, especially when coupled with renewable sources and adequate technology [11–14], and it is used in a variety of applications [15–17].

Within the HyS cycle, it is well known that transition metals, even in trace amounts, are needed to catalyse the SO_2 oxidation reaction [18–20]. The current catalyst of choice is platinum (Pt), a rare and very expensive noble metal. While various other metals have been investigated [21], including Cu [22–25], Ni [26–28], Ag [29,30], Rh [31,32], Pd [24,32–36], in addition to Pt [24,31,37–40], which is still the best performing catalyst in terms of activity and stability [41–43]. However, major difficulties are still experienced in experiments, in part due to the occurrence of various co-adsorbed surface sulphur species, including elemental sulphur (S), sulphur oxide (SO) and sulphur trioxide (SO_3), amongst others [9].

Although sulphur an essential element and the fifth most common element on Earth [3,44], its presence in a catalytic environment is detrimental, causing lower yields in production and catalyst poisoning [45]. However, very little work has been performed on evaluating the energetics or thermodynamics of the adsorption of sulphur or sulphur oxides on catalyst surfaces or their surface reactions. In this paper, we have used density functional theory (DFT) calculations to predict the behaviour of S, SO and SO_3 on the Pt (001), (011) and (111) surfaces. We have examined the geometric and electronic properties of the systems, including the most stable adsorption sites, adsorption modes and possible desorption of species that may occur, before considering increased surface coverages. Thermodynamic surface phase diagrams have also been generated by taking into consideration the surface free energies and the chemical potentials of $SO_{x,\,(x=0,1,3)}$.

2. Computational Methods

2.1 Calculation Methods

Similar to the method used to study the adsorption of H_2O and SO_2 [46–48], the Vienna Ab Initio Simulation Package (VASP) [49–52] version 5.4.1 was used to simulate the Pt surfaces and their interaction with S, SO and SO_3. In all calculations, the projector augmented wave (PAW) [53,54] pseudopotential was used to describe the interaction between the valence and core electrons. The core electrons were defined up to and including 5p, 3p and 1s orbitals for the Pt, S and O atoms, respectively. The exchange-correlation approximation was included with the Perdew-Burke-Ernzerhof (PBE) [55] functional within the generalised gradient approximation (GGA), including the D3-BJ method by Grimme with Becke-Johnson damping [56] to account for the long-range dispersion interactions [57–61] in these surface-adsorbate systems. Plane waves were included with the recommended cut-off of 400 eV. The conjugate gradient technique was adopted for all geometry optimisations and to ensure an electronic entropy of less than 1 meV.atom^{-1}, whereas a smearing of 0.05 eV with the Methfessel-Paxton scheme order 1 [62] was used to determine the partial occupancies during geometry optimisation. The final static simulations were obtained with the tetrahedron method with Blöchl corrections [63] to ensure accurate total energies, charges and densities of states, where the electronic and ionic optimisation criteria were set at 10^{-5} eV and 10^{-2} eV.Å^{-1}, respectively.

The $Fm\bar{3}m$ crystal structure [64] of Pt was used to construct a bulk Pt structure within a primitive face-centred cubic (*fcc*) cell. The *k*-point mesh for these calculations was a *Γ*-centred 17 x 17 x 17 Monkhorst-Pack mesh [65]. The resulting *fcc* Pt lattice constant was 3.926 Å, which correlates with the experimental value of 3.925 Å [66,67]. The low Miller index Pt (001), (011) and (111) surfaces were created with the METADISE code [68]. Periodic p(3 x 3), p(3 x 3) and p(4 x 4) supercells were constructed, respectively, each with four layers and a 15 Å vacuum space to ensure that no interaction would occur between the adsorbates and surfaces in neighbouring simulation cells deriving from the 3-dimensional boundary conditions. All three surfaces are bulk terminated 2x2 structures with four atomic layers, with the surface simulation cells containing 72, 72 and 64 atoms respectively. The Brillouin zone was sampled by a *Γ*-centred 7 x 7 x 1 Monkhorst-Pack *k*-point grid. During the optimisation of the surfaces, the bottom two layers of the supercells were frozen in their bulk locations, with the remaining two layers allowed to move until the set energy criteria were met. Even though Pt does not have unpaired electrons, spin polarisation was considered during these surface calculations, as future work will also include base metals dopants like Ni and Co, for which this would be necessary.

For the calculations of the geometrical properties, adsorption and electronic properties, the isolated S, SO and SO_3 molecules were modelled in a periodic box of 12 x 13 x 14 Å to ensure negligible interaction with neighbouring cells. For both the geometry optimisations and energy calculations, the Gaussian

smearing [62] of 0.05 eV scheme was used with a *Γ*-centred Monkhorst-Pack [65] *k*-point mesh of 1 x 1 x 1. None of the adsorbate molecules were computed with symmetry constraints, but for increased accuracy, dipole corrections were added in all directions. Spin polarisation was considered both for the isolated molecules and in the adsorption calculations. The breakdown of charge transfer between the adsorbates and the surfaces was obtained via the Bader analysis [69–72], assigning electron density of molecules and solids to individual atoms or regions enclosed by local minima in the charge density.

2.2 Coverage-dependent Surface Energies

The standard calculation [58,73] of the surface energies for relaxed and unrelaxed systems was used. To calculate the average adsorption energy (E_{ads}) per adsorbate molecule (S, SO and SO_3) adsorbed onto the Pt surface, the following equation (1) was used [46–48,74]:

$$E_{ads} = \frac{1}{N_{SO_x}}\left[E_{Pt,r}^{N_{SO_x}\neq 0} - \left(E_{Pt,r}^{N_{SO_x}=0} + N_{SO_x}E_{SO_x}\right)\right], x = 0, 1, 3 \quad (1)$$

where N_{SO_x} is the number of adsorbed S, SO or SO_3 molecules, $E_{Pt}^{N_{SOx}\neq 0}$ is the energy of the Pt slab with adsorbed SO_x molecules, $E_{Pt}^{N_{SOx}=0}$ is the energy of the clean Pt surface, and E_{SO_x} is the energy of the isolated $SO_{x,\,(x = 0, 1, 3)}$ molecule after relaxation. Another measure of adsorption is the energy of sequential adsorption (Sequential E_{ads}),[47] indicating the difference in energy as coverage increases:

$$Seq.E_{ads} = \left[E_{Pt,r}^{N_{SO_x}\neq 0_{(i+1)}} - \left(E_{Pt,r}^{N_{SO_x}\neq 0_i} + E_{SO_x}\right)\right], x = 0, 1, 3, i = 0, 1, \ldots N \quad (2)$$

thereby calculating the energy difference between that of an adsorbate system with one more adsorbate $E_{Pt}^{N_{SOx}\neq 0_{(i+1)}}$ from the previous system with one less adsorbate ($E_{Pt}^{N_{SOx}\neq 0_{(i)}}$).

The surface coverage (θ) is defined as the number of adsorbed SO_x molecules (N_{SO_x}) divided by the number of adsorption sites (N), as denoted by

$$\theta = \frac{N_{SOx}}{N} \quad (3)$$

If no adsorption has taken place, θ = 0, whereas for full coverage, i.e. when a monolayer has formed on the surface, θ = 1. The most stable configurations of the (001), (011) and (111) surfaces were used to investigate surface coverage, with the surface simulation cells having 9, 18 and 9 adsorption sites (N), respectively. To incorporate the thermodynamics effect of the different coverages of $SO_{x,\,(x = 0, 1, 3)}$ on the Pt (001), (011) and (111) surfaces, the correlating surface free energies (σ) are compared at different temperatures (T) and the $SO_{x,\,(0,\,1,\,3)}$ chemical potential (μ_{SOx}). To this end, we have followed an

established method [74] to determine the thermodynamic effect of the adsorption of SO_2 [47,48] and H_2O [46] on these Pt surfaces. The resulting change in surface free energy resulting from the SO_x adsorption was calculated as follows:

$$\Delta\sigma(T,p) = \frac{1}{A_{surface}} \left[E_{Pt,r}^{N_{SO_x}\neq 0} - E_{Pt,r}^{N_{SO_x}=0} - N_{SO_x}.\mu_{SO_x}\right] \quad (4)$$

In order to calculate the surface free energy as a function of temperature and pressure, we also require the chemical potential of the SO_x species $\mu_{SO_x}(T,p_0)$, which we have obtained from experimental values [46–48], by extracting the chemical potential from ideal gas values in thermodynamic tables [75]. The chemical potential of $SO_{x,\,(x\,=\,0,\,1,\,3)}$ species in the gas phase has been reported before [76] and can be expressed as:

$$\mu_{SO_x}(T,p) = E_{SO_x}^{ZPE} + \Delta G_{SO_x}(T,p_0) + k_B T ln\frac{p}{p_0} \quad (5)$$

Where the zero-point energy $E_{SO_x}^{ZPE}$ includes the contributions from rotation and vibrations of the SO_x molecule, and the Gibbs free energy difference $\Delta G_{SOx}(T,p_0)$ is per SO_x molecule for temperatures between 0 K and T, at p_0 = 1 bar. The final term ($k_B T ln\frac{p}{p_0}$) denotes the free energy change of SO_x gas at constant temperature (T) when the partial pressure changes from p_0 to p.

3. Results and Discussion

3.1 Pt (001), (011) and (111) surfaces

Figure 1 shows the three Pt surfaces under consideration with possible adsorption sites for each surface. The *fcc* arrangement of Pt resulted in the flat smooth Pt (001) and Pt (111) structures and a corrugated or grooved Pt (011) surface. The surface energy of each surface correlates with experimental [77] and modelled values [78] and followed the observed trend Pt (111) < Pt (001) < Pt (011) at 2.046 J/m^2, 2.462 and 2.615 J/m^2, respectively. Both the Pt (001) and Pt (011) have three adsorption sites, indicated by atop (A), bridge (B) and four-fold hollow (4F), while the Pt (111) has four sites indicated by atop (A), bridge (B), face-cubic centred (*fcc*) and hexagonal close packed (*hcp*). All the Pt atoms throughout this paper, is gold coloured, but for clarity the second layer atoms below the top surface are displayed in a lighter colour.

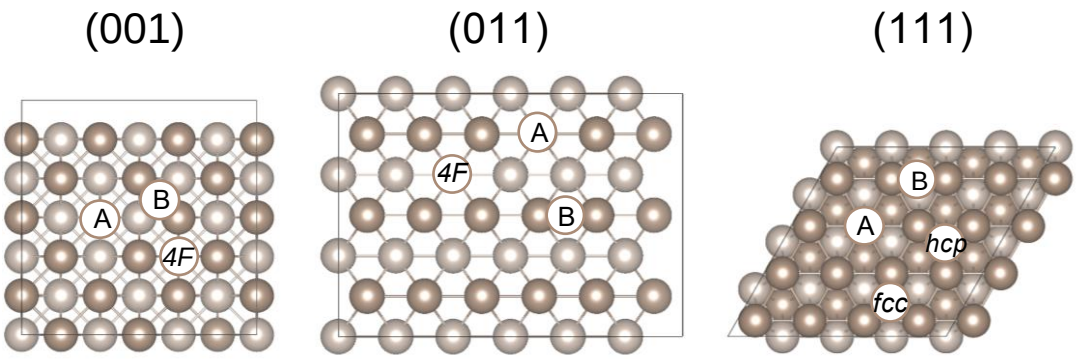

Figure 1 – Top views of the Pt (001), (011) and (111) surfaces, with the adsorption sites indicated as four-fold hollow (4F), bridge (B) and atop (A), face-cubic centred (*fcc*) and hexagonal close packed (*hcp*). All Pt atoms are gold in colour throughout the paper, with the second layer in a lighter colour to distinguish between top layer and subsequent layer atoms.

3.2 S Adsorption and Surface Coverage

Only one atom of elemental sulphur (S) was considered for adsorption in all adsorption sites on all three Pt surfaces. The most stable adsorptions are shown in Figure 2, with the adsorption energies (E_{ads}), charge transfer and bond distance (d) of the adsorbed S on the Pt (001), (011) and (111) surfaces listed in Table 1. The most stable adsorption with regard to adsorption energy was on the Pt (001) surface at −7.09 eV, followed by both the Pt (011) and Pt (111) with adsorption energies ranging between −5.1 and −5.5 eV. Alfonso [79] also showed that the most stable S adsorption on the Pt (111) occurs in the *fcc* site (−5.23 eV) followed by the *hcp* site (−5.03 eV). In both the Pt (001) and Pt (011) surfaces, the S atom prefers the 4F hollow adsorption site, whereas on the (111) surface, both the *fcc* and *hcp* hollow is preferred. Rodríguez and Santana [80] have shown that S adsorption is most stable on the $(100)_{4F}$ surface (−5.16 eV), followed by $(111)_{fcc}$ surface (−4.63 eV) and then the (110) surface (−4.37 eV), however in the B site rather than the 4F binding site. From the charge analysis in Table 1, the negative values of Δq indicate charge transfer from the surface to the adsorbate, where most charge was transferred to the $(011)_{4F}$ site, followed by $(111)_{hcp}$, $(011)_{B}$, $(011)_{4F}$ and $(111)_{fcc}$. Interestingly, in the of the $(001)_{4F}$, $(011)_{B}$ and $(111)_{fcc}$ sites, S is surrounded by various Pt atoms in the surface, but none in the second layer just below the S atom, whereas in the $(011)_{4F}$ and $(111)_{hcp}$ sites, a Pt atom in the second layer is located below the S atom, contributing to the higher electron transfer observed (Table 1). The adsorption energy for $N_S = 1$ was calculated to be most favourable on the (001) surface, followed by the (011) and (111) surfaces, which is the same trend as was found for H_2O and SO_2 adsorption [46–48].

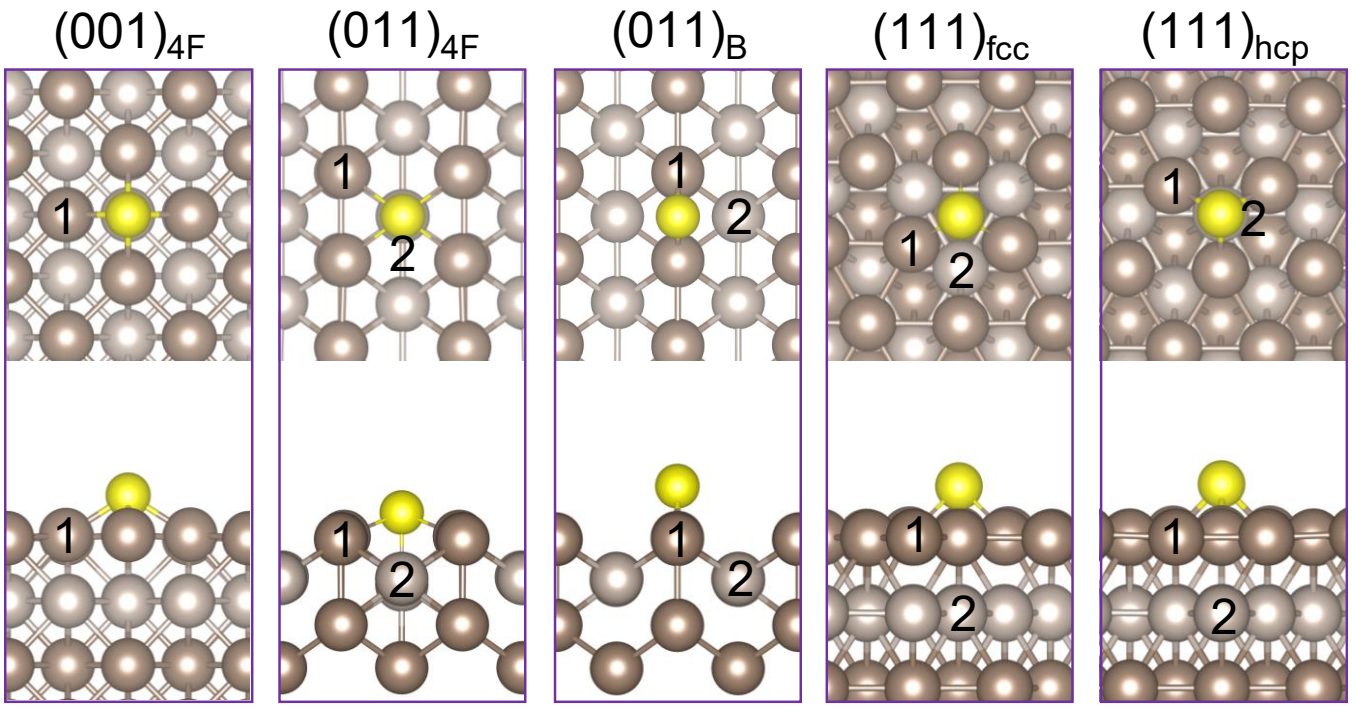

Figure 2 – Stable absorption sites of S on Pt (001), (011) and (111) surfaces. The atom colour yellow denotes sulphur atoms. The numbers (1, 2) in the figure indicate the significant Pt atoms in the surface (1) or in the second layer (2).

Table 1 – Adsorption energies (E_{ads}), charge transfer and bond distance (d) of the adsorbed S on the Pt (001), (011) and (111) surfaces, with $\theta_{(001)/(111)} = 0.11$, $\theta_{(011)} = 0.06$. The numbers (Pt_1, Pt_2) indicates the significant Pt atoms in the surface or in the second layer, as shown in Figure 2..

		$(001)_{4F}$	$(011)_{4F}$	$(011)_B$	$(111)_{fcc}$	$(111)_{hcp}$
	E_{ads} (eV)	−7.09	−5.47	−5.14	−5.47	−5.26
	Δq (e)	−0.07	−0.25	−0.08	−0.06	−0.18
d (Å)	S-Pt_1	2.35	2.46	2.20	2.26	2.26
	S-Pt_2	-	2.34	3.61	4.14	3.87

The most stable configurations ($(001)_{4F}$, $(011)_{4F}$ and $(111)_{fcc}$) were used to investigate surface coverage, by increasing the number of adsorbed S atoms ($N_{SO_x}, x = 0$) on each Pt surface until a monolayer (ML) was obtained. To obtain the lowest energy configurations, shown in Figure 3, various placements of subsequent S atoms were considered. To determine if adsorption is still favoured as the surface coverage increases, the average adsorption energy as a function of the surface coverage is shown in Figure 4(a), whereas the sequential adsorption energy as a function of surface coverage is shown in Figure 4(b).

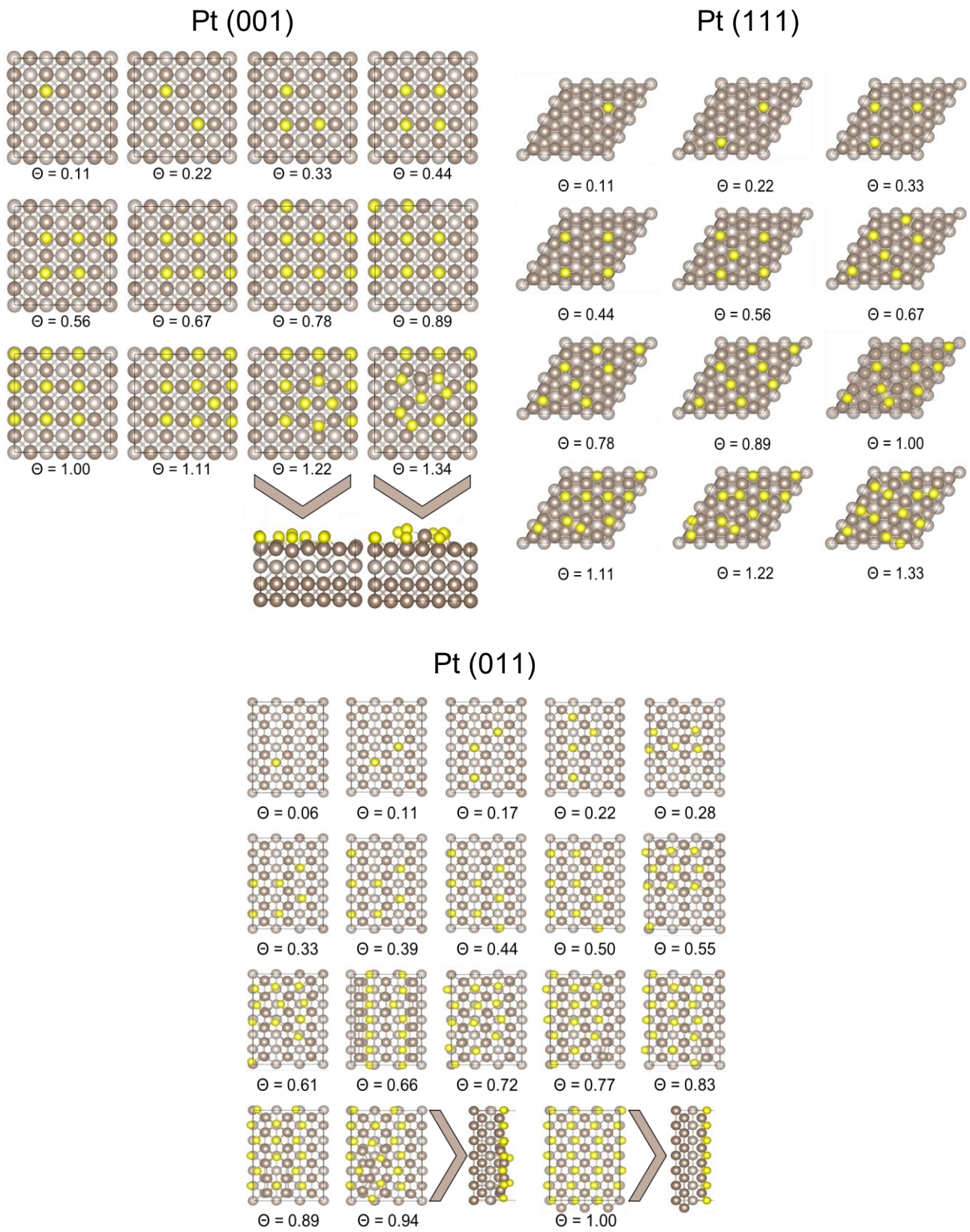

Figure 3 – Increased adsorption coverage of S on Pt (001), (011) and (111) surfaces.

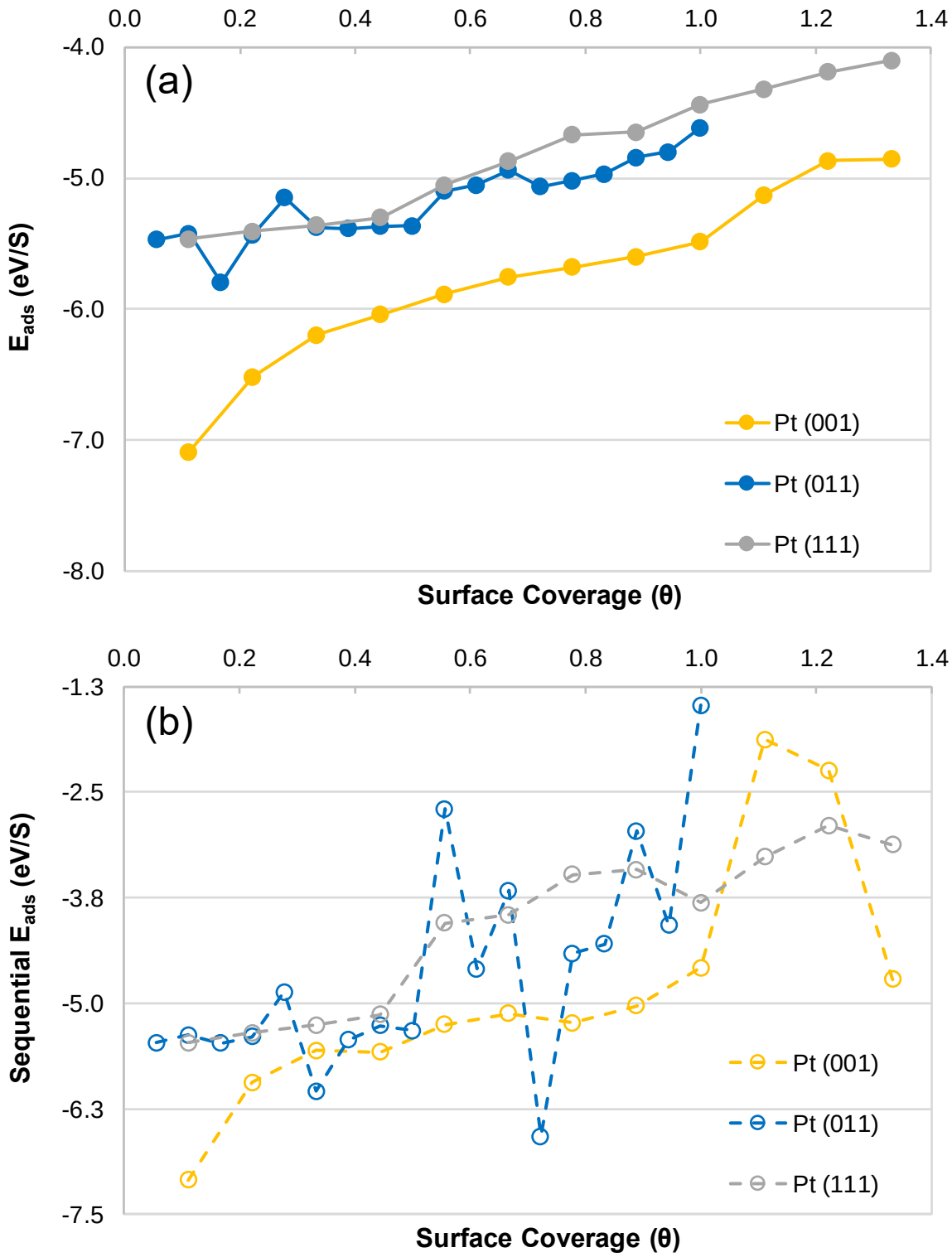

198

199 Figure 4 – Average (a) and sequential (b) adsorption energies (E_{ads}) as a function of the S surface
200 coverage (θ) on the Pt (001), (011) and (111) surfaces.

201

Not surprisingly, more S atoms could be adsorbed onto the Pt surfaces, than H_2O [46] or SO_2 [47] molecules. On the (001) surface, as the surface coverage increases up to θ = 1.11, the mode of adsorption remained the same; no recombination occurs during the geometry optimisations. However, as the coverage increased to θ = 1.22, the surface became 'crowded' and the S atoms are no longer perfectly adsorbed in the 4F hollow. At θ = 1.34, the S atoms surrounded one of the surface Pt atoms and displaced it out of the surface plane and two S_2 molecules formed on the surface. This behaviour confirms experimental reports [9] that Pt electrodes are poisoned and in extreme cases delamination of Pt occurs when S deposition is detected on the surface. The average adsorption energy is calculated as a function of the surface coverage of S, i.e. the total adsorption energy divided by the maximum number of binding sites, i.e. 9, 18, 9 for the (001), (011) and (111) surface, respectively. Figure 4(a) shows that the same trend is observed as in previous studies on H_2O and SO_2 adsorption, where the E_{ads} decreases with increased θ. The sequential adsorption also shows that up to θ = 1.11, E_{ads} decrease. However, at higher coverages θ ≥ 1.22, the E_{ads} increases due the formation of S_2. Also, as the Pt is displaced into the vacuum, the surface becomes more unstable and less active, which can also cause the E_{ads} to increase.

On the (011) surface, when adsorption was increased to θ = 1, no S recombination or Pt delamination occurred. At θ > 1, a second layer of S started to form, showing that the (011) surface was less reactive. Similar to the (001) surface, the average E_{ads} decreases with increasing θ, but the sequential E_{ads} did not show a clear trend.

The Pt (111) surface showed no reactivity or delamination up to θ = 0.89. However, when all 9 *fcc* sites were filled (θ = 1), S started to adsorb onto the *hcp* sites, resulting in the formation of S_2. More pairs of S_2 formed as the S adsorption continued up to θ = 1.33. Higher coverage was not obtained, however, as a second layer started forming. Due to the formation of S_2, not all the S atoms were adsorbed onto the *fcc* sites and no Pt displacement was observed. Similar to the other two surfaces, the E_{ads} increased as θ increased, which was also observed in the sequential E_{ads} data. With the formation of the S_2 molecules, E_{ads} increased slightly.

Comparing the increase in coverage on all three Pt surfaces, it was seen that the highest coverage of S was obtained on the (001) and (111) surfaces, followed by the (011) surface. Also, both the (001) and (111) surfaces were reactive towards the formation of S_2 and Pt degradation.

3.3 SO Adsorption and Surface Coverage

Three modes of SO adsorption on the metallic surfaces have been investigated, including S-bound, O-bound and S,O-bound on all the adsorption sites shown in Figure 1. The most stable structures for the

SO adsorption on the Pt surface in terms of adsorption energy are shown in Figure 5. The correlating adsorption energy, bond distances and angles and charge transfer of the adsorbed SO, with respect to the Pt surfaces, are shown in Table 2.

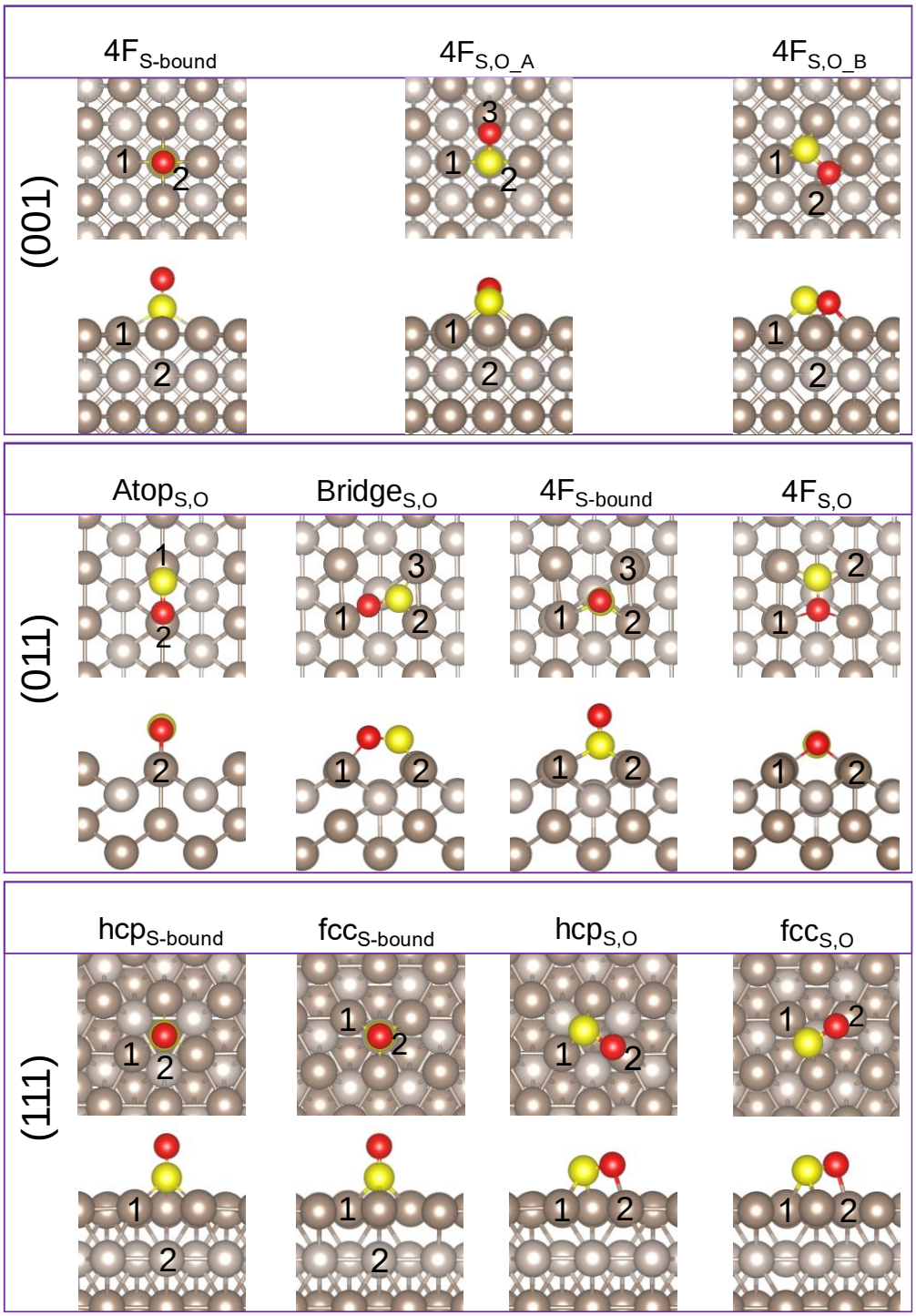

Figure 5 – Stable absorption sites of SO on Pt (001), (011) and (111) surfaces. The atom colours yellow and red denotes sulphur and oxygen atoms, respectively. The numbers (1, 2) in the figure indicate the significant Pt atoms in the surface (1) or in the second layer (2).

Table 2 – Adsorption energies (E_{ads}), bond distance (d) and angles (∠) of the adsorbed SO on the Pt (001), (011) and (111) surfaces, with the relevant charge transfers (Δq) following adsorption, with $\theta_{(001)/(111)} = 0.11$, $\theta_{(011)} = 0.06$. The numbers (Pt_1, Pt_2) indicate the significant Pt atoms n the surface or in the second layer shown in Figure 5.

		(001)			(011)				(111)			
		$4F_S$	$4F_{S,O\_A}$	$4F_{S,O\_B}$	$Atop_{S,O}$	$Bridge_{S,O}$	$4F_S$	$4F_{S,O}$	hcp_{S}	fcc_{S}	$hcp\_{S,O}$	$fcc\_{S,O}$
	E_{ads} (eV)	−5.10	−4.83	−4.12	−3.01	−3.56	−3.17	−3.57	−3.39	−3.25	−3.19	−3.10
	Δq (e)	−0.07	−0.21	−0.41	−0.17	−0.21	−0.07	−0.26	−0.17	−0.12	−0.25	−0.23
d (Å)	S-Pt_1	2.33	2.32	2.23	2.15	3.35, 2.30(Pt_3)	2.38, 2.43(Pt_3)	3.19	2.23	2.23	2.26	2.26
	S-Pt_2	3.35	3.58	3.10	2.97	2.21	2.25	2.26	4.10	3.84	2.85	2.85
	O-Pt	3.35 (Pt_1)	2.10 (Pt_3)	2.19 (Pt_2)	2.06 (Pt_2)	2.15 (Pt_1)	2.31 (Pt_1)	2.40 (Pt_1)	3.35 (Pt_1)	3.37 (Pt_1)	2.15 (Pt_2)	2.18 (Pt_2)
	S-O	1.47	1.60	1.67	1.58	1.57	1.48	1.63	1.46	1.46	1.56	1.56
∠ (°)	O-S-Pt	121.8 (Pt_1)	103.12 (Pt_1)	103.6 (Pt_1)	106.1 (Pt_1)	112.1 (Pt_2)	115.9 (Pt_1)	104.3 (Pt_2)	129.2 (Pt_1)	130.8 (Pt_1)	106.8 (Pt_1)	105.2 (Pt_1)
	SO-$surf_{\perp}$	89.7	21.02	79.6	16.1	14.9	2.7	91.6	92.6	93.4	30.4	32.2

Three stable SO adsorption configurations were obtained for the (001) surface. All three were on the 4F binding site, with the highest adsorption energy achieved where S was bound to the Pt surface and the O directed away, i.e. $4F_{S\text{-bound}}$, followed by two configurations where both S and O were bound to Pt. In the first configuration, $4F_{S,O\_A}$, the S atom is bound to two Pt atoms on opposite sides of the 4F hollow, with the O atom bound to a third Pt atom; in the second configuration, $4F_{S,O\_B}$, both the S and O atoms are bound to two Pt atoms on either side of the 4F hollow, as shown in Figure 5. We note that the charge transfer is lowest (−0.07 e^-) when only one S is bound to the Pt surface, followed by the tri-bound $4F_{S,O\_A}$ (−0.21 e^-) and the tetra-bound $4F_{S,O\_A}$ (−0.41 e^-) configurations. When comparing the S-O bond length, it can be seen that the adsorption configuration can cause a deviation of up to 0.2 Å from the experimentally measured S-O bond length of 1.44 Å [81], which correlates with the $4F_{S\text{-bound}}$ structure. This shows that the bond lengths and charge transfer are dependent on the bond order and type of bonds formed during adsorption. [82]

On the Pt (011) surface four stable adsorption configurations were observed, one being S-bound and three S,O-bound. Energetically, the most stable is the tetra-bound configuration $4F_{S,O}$, within a 4F hollow, following the groove on the (011) surface, closely followed by the tri-bound $Bridge_{S,O}$ where SO is again in the 4F hollow, but across the (011) groove. The third most stable configuration is the $4F_{S\text{-bound}}$, with a bidentate S offset from the 4F hollow, followed by the fourth configuration, $Atop_{S,O}$ where S,O forms a bidentate configuration on the ridge of the (011) surface between two Pt atoms, as shown in Figure 5. Similar to the (001) surface, the charge transfer is dependent on the bond orders $4F_{S,O}$ (4) > $Bridge_{S,O}$ (3) > $4F_{S\_bound}$ (2) > $Atop_{S,O}$ (2). As on the (001) surface, the S-O bond length of $4F_{S\text{-bound}}$ correlates with the free S-O bond length, but in the other cases deviates by up to 0.15 Å, [81] depending on the adsorption configuration.

The (111) surface achieved four stable adsorption configurations, either with a S,O-bonded or S-bound geometry on both the *fcc* and *hcp* binding sites, i.e. $fcc_{S,O}$, $fcc_{S\text{-bound}}$, $hcp_{S,O}$ and $hcp_{S\text{-bound}}$, respectively. Similar to the (001) surface, the adsorption energy was the highest for the S-bound configurations, $hcp_{S\text{-bound}}$ > $fcc_{S\text{-bound}}$, followed by the S,O-bound configurations, $hcp_{S,O}$ > $fcc_{S,O}$. Similar to the trends observed on both the (001) and (011) surfaces, the charge transfer increased as the bond order increased, $fcc_{S\text{-bound}}$. < $hcp_{S\text{-bound}}$ < $fcc_{S,O}$ < $hcp_{S,O}$. As on the (011) surface, the S-O bond length of S-bound configurations ($fcc_{S\text{-bound}}$. and $hcp_{S\text{-bound}}$) correlates with the free S-O bond length, but it is elongated by 0.1 Å in the S,O-bound configurations ($fcc_{S,O}$ and $hcp_{S,O}$).

Similar to the adsorption of S, H_2O and SO_2, the adsorption energy for $N_{SO} = 1$ was calculated to be most favourable on the (001) surface, followed by the (011) and (111) surfaces [46–48]. The most stable SO configurations on all three Pt surfaces were used to investigate the effect of surface coverage. However,

on the (011) surface, the $4F_{S,O}$ and $Bridge_{S,O}$ had similar adsorption energies, and thus, the four configurations considered included $(001)_{4F\_S}$, $(011)_{4F\_S,O}$, $(011)_{B\_S,O}$ and $(111)_{hcp\_S}$, shown in Figure 6.

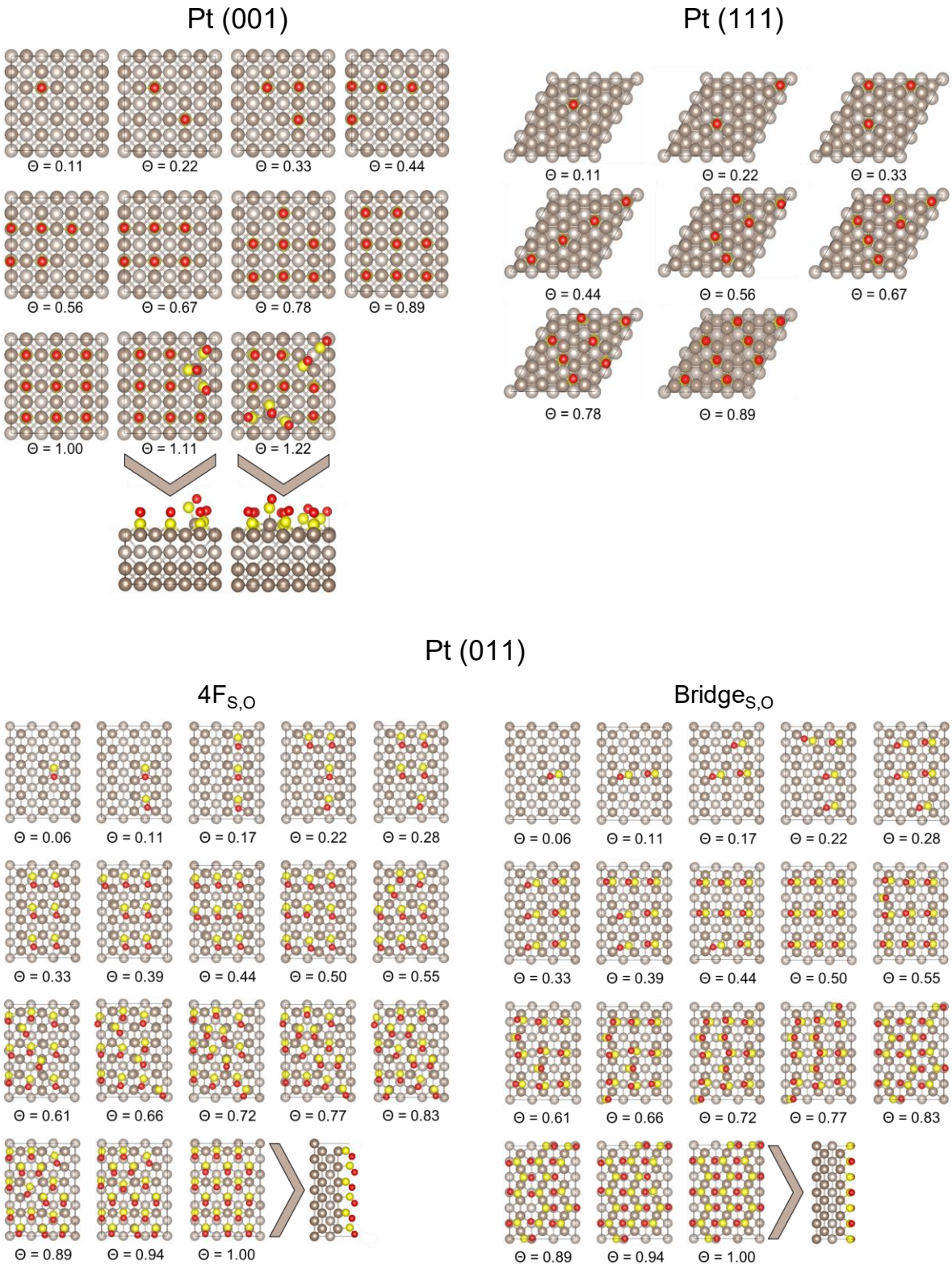

Figure 6 – Increased SO coverage on the Pt (001), (011) and (111) surfaces.

As with the adsorption of S, the number of adsorbed SO molecules ($N_{SO_x}, x = 1$) is increased on each Pt surface, until a monolayer was obtained. Figure 7 shows the corresponding surface coverage as a function of both adsorption energy (a) and sequential adsorption energy (b). As with the adsorption of elemental S, it can be seen that on the Pt (001) the E_{ads} decreases steadily as the surface coverage is increased, in correlation with the sequential E_{ads} up to θ = 1. At this stage, all the 4F hollow adsorption sites are occupied and very stable. However at θ = 1.11, one of the SO molecules is bound atop a Pt atom which is pulled out from the surface, causing the sequential E_{ads} to decrease. When a second SO molecule was added in the atop site, again a Pt atom was displaced from the surface, indicating that it is not only elemental S which causes Pt delamination in a catalytic environment, but that the presence of SO can also cause surface destabilisation and possibly catalyst degradation. At θ > 1.22, a second layer of SO started to form, but there was no evidence that SO molecules reacted with each other.

As on the (001) surface, on the Pt (011) surface E_{ads} decreased linearly as θ increased for both the $4F_{S,O}$ and $Bridge_{S,O}$ adsorption configurations until full coverage (θ = 1) was obtained. Comparing the sequential E_{ads} for both these adsorption, it can be seen that in the $4F_{S,O}$ case E_{ads} plateaus up to a coverage of θ = 0.55. At coverages 0.55 < θ < 0.73, the surface becomes crowded, causing the sequential E_{ads} to decrease significantly, due to a change in SO adsorption. However, at θ = 0.77 the sequential E_{ads} increased sharply, due to all the SO molecules aligning in a similar fashion to the single SO adsorption configuration. At θ = 1, all the adsorption sites are occupied and stable. Coverages of θ > 1 were not observed, as a second layer started to form. Similar to the (001) surface, no reaction between sequential SO molecules were observed on the Pt (011) surface. In the case of the increased surface coverage of $Bridge_{S,O}$ both the E_{ads} and sequential E_{ads} decreased as N_{SO} increased. In this case the adsorption configuration stayed very similar to the single SO adsorption. Higher coverage than θ > 1 was not obtained as a second layer started to form. Again, no reaction between the SO molecules was observed.

Similar to the other surfaces, the (111) surface showed a steady decrease in E_{ads} and sequential E_{ads} as θ increased. At θ = 1, all hcp sites were occupied by SO, but as an additional SO was placed on an *fcc* site, a second SO layer started to form. As with the other surfaces, the subsequent addition of SO molecules did not lead to additional reactions.

Comparing the increased coverage on all three Pt surfaces, it was seen that the highest coverage of SO was achieved on the (001) surface, followed by the (011) and then (111) surfaces.

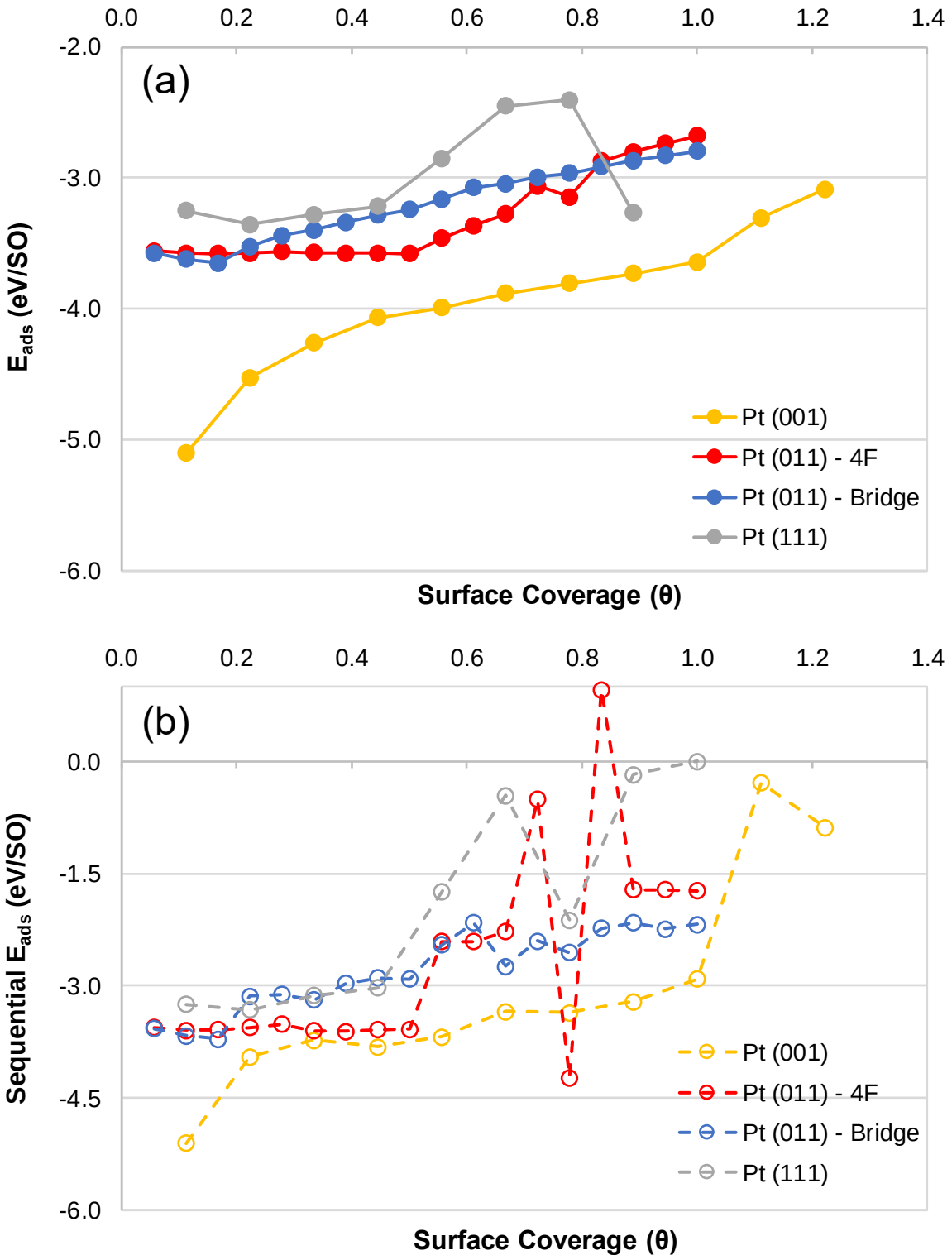

313

314 Figure 7 – Average (a) and sequential (b) adsorption energies (E_{ads}) as a function of the SO surface
315 coverage (nm^{-2} Pt) on the Pt (001), (011) and (111) surfaces.

316

3.4 SO_3 Adsorption and Surface Coverage

The literature has shown [19] that five modes of SO_3 adsorption are possible and all were considered in this work, including (i) planar O,O,O, where all four atoms are parallel to the surface, (ii) S,O,O, where only two S-O interact with the surface, (iii) O,O where only two of the O atoms interact, (iv) S,O where one S-O bond interact with the surface and the other two O atoms are directed away from the surface and (v) where only one O atom interacts with the surface. All five modes were investigated in the various adsorption sites shown in Figure 1. The most stable structures found for the adsorption of SO_3 onto the Pt surface are shown in Figure 8, with the adsorption energies, charge transfer, bond distances and angles of the adsorbed SO_3 with respect to the Pt surfaces listed in Table 3.

On the (001) surface, two stable configurations were observed, the most stable being $4F_{S\text{-}bound}$, where the S atom is bound within a 4F hollow, and two O atoms bind to two Pt atoms of the 4F hollow with the third O atom directed towards the vacuum. The second adsorption mode is $Atop_{O,O,O}$, where again the S atom is in the 4F hollow and all three O atoms are bound atop a Pt atom of the 4F hollow. The literature has shown that on the α-Fe_2O_3 (001) surface [83], an O,O-bridge formed on the surface with a binding energy between −2.27 and −2.46 eV, depending on whether the bridge formed over a Fe-O or Fe-Fe binding site, respectively. Similar to the adsorption of SO on (001), the charge transfer increased as the bond order increased. The free SO_3 molecule showed an average S-O bond length of 1.47 Å and an O-S-O bond angle of 120°, which correlates with the free S-O(1) bond length in the $4F_{S\text{-}bound}$ configuration. In both $4F_{S\text{-}bound}$ and $Atop_{O,O,O}$, the Pt-bound S-O bonds are stretched on average by 0.1 Å. In the $4F_{S\text{-}bound}$ configuration, the planar SO_3 changed to a nearly tetrahedral configuration, causing the O-S-O bond angles to decrease. Also in the $Atop_{O,O,O}$ configuration, with the O atoms bound atop the Pt atoms, the S atom is pushed slightly out of plane, decreasing the O-S-O bond angles, which confirms a tetrahedral configuration and indicates that SO_3 is chemisorbed onto the (001) surface.

On the (011) surface, three stable adsorption modes were observed, $4F_{S,O}$, $4F_{O,O,O}$ and $4F_{O,O\text{-}bridge}$. In the first configuration ($4F_{S,O}$), the S atom is bound to one Pt atom on the ridge, one S-O(1) formed a bridge across the (011) ridge and the other S-O(3) formed a bridge on the (011) ridge and oxygen O(2) is directed towards the vacuum. The second stable configuration ($4F_{O,O,O}$), S was over the 4F hollow, with all three O atoms bound to the Pt atoms of the 4F hollow, forming two S-O bridges across the (011) ridge. Similarly, in the third stable configuration ($4F_{O,O\text{-}bridge}$) S was over the 4F hollow forming two S-O bridges across the (011) ridge, with O(3) directed along the groove of the (011) surface. It has been shown [83] on the α-Fe_2O_3 (001) surface, that Fe-O-Fe binding causes ridges and valleys similar to the (011) surface and on these Fe-O-Fe binding site, SO_3 forms a stable O,O-bridge across the surface, similar to our $4F_{O,O\text{-}bridge}$ configuration, with a binding energy of −2.27 eV.

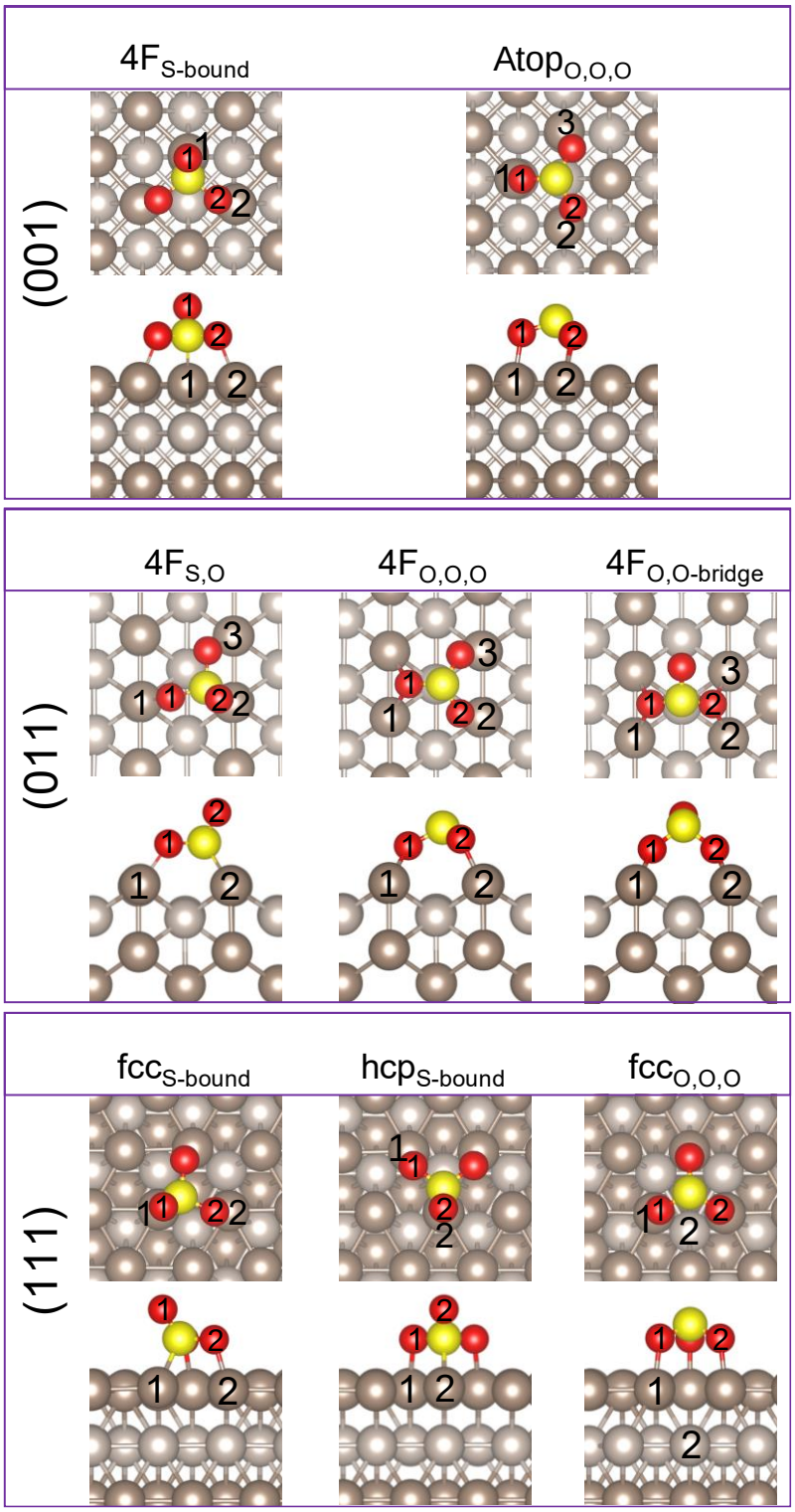

Figure 8 – Stable absorption sites of SO_3 on Pt (001), (011) and (111) surfaces. The atom colours yellow and red denotes sulphur and oxygen atoms, respectively. The numbers (1, 2) in the figure indicate the significant Pt or oxygen atoms in the surface (1) or in the second layer (2).

Table 3 – Adsorption energies (E_{ads}), bond distance (d) and angles (∠) of the adsorbed SO_3 on the Pt (001), (011) and (111) surfaces, with the relevant charge transfers (Δq) following adsorption, with $\theta_{(001)/(111)} = 0.11$, $\theta_{(011)} = 0.06$. The numbers (Pt_1, Pt_2, O_1, O_2, O_3) indicate the significant Pt and O atoms shown in Figure 8.

		(001)		(011)			(111)		
		$4F_S$	$Atop_{O,O,O}$	$4F_{S,O,O}$	$4F_{O,O,O}$	$4F_{O,O\text{-}bridge}$	fcc_{S}	hcp_{S}	$fcc\_{O,O,O}$
	E_{ads} (eV)	−3.38	−2.95	−2.68	−2.18	−1.39	−1.83	−1.79	−1.59
	Δq (e)	−0.60	−0.84	−0.64	−0.86	−0.88	−0.58	−0.57	−0.83
d (Å)	S-Pt_1	2.23	3.12	3.26	3.50	3.55	2.27	2.94	3.16
	S-Pt_2	3.03	3.27	2.23	3.22	3.55	2.95	2.26	3.16
	O_1-Pt_1	3.20	2.10	2.08	2.24	2.18	3.22	2.14	2.11
	O_2-Pt_2	2.10	2.11	3.14	2.10	2.18	2.12	3.23	2.11
	S-O_1	1.44	1.54	1.55	1.62	1.64	1.44	1.54	1.55
	S-O_2	1.55	1.56	1.45	1.53	1.64	1.54	1.44	1.54
∠ (°)	O_1-S-O_2	110.2	106.8	108.0	106.6	105.8	111.1	111.1	107.2
	O_2-S-O_3	107.5	107.6	110.9	108.9	105.2	106.6	107.1	107.2

The charge transfer between SO_3 and the (011) Pt surface did not follow the same bond order trend as observed for the other adsorptions. Interestingly, more electrons were transferred when either just two or all three O atoms were bound to the Pt surface ($4F_{O,O\text{-bridge}}$ and $4F_{O,O,O}$, respectively), compared to when two O and one S atom were bound ($4F_{S,O}$). As observed on the (001) surface, the bound SO_3 configuration changes to a tetrahedral mode, elongating the bound S-O bonds and decreasing the O-S-O bonds, again indicating that SO_3 is chemisorbed onto the (011) surface.

On the (111) surface, three stable adsorption modes were observed, including $fcc_{S\text{-bound}}$, $hcp_{S\text{-bound}}$ and $fcc_{O,O,O}$. The first two are similar, where S is bound over either an *fcc* or *hcp* hollow, with O atoms atop two of the Pt atoms of the hollow adsorption site. In the third adsorption configuration, $fcc_{O,O,O}$, S is again over an *fcc* hollow, with all three O atoms bound atop the surrounding Pt atoms. The $fcc_{S\text{-bound}}$ configuration is similar to our previously predicted SO_2 adsorption on the (111) surface [47], which had an S,O-bonded geometry on the *fcc* binding site, with one S-O bond in the plane of the surface and the other oxygen directed away from the surface. Lin and co-workers [19] also showed that various adsorption configurations are possible on the (111) surface, with the $fcc_{S\text{-bound}}$ being the most stable with a binding energy of 1.43 eV. They have also shown that the Pt bound S-O bond length is elongated (1.56 Å), while the non-surface bound S-O is similar to the gas phase bond length of S-O (1.46 Å) with a decreased O-S-O bond angle (107°). Similar to the (001) surface, the charge transfer increased as the bond order increased, i.e. $fcc_{S\text{-bound}} > hcp_{S\text{-bound}} > fcc_{O,O,O}$. Chemisorption of SO_3 occurred for all three configurations, similar to the (001) and (011) surfaces, the Pt bound S-O bond lengths increased and the O-S-O bond angles decreased.

Similar to the adsorption of S, SO, H_2O and SO_2, the adsorption energy for $N_{SO_3} = 1$ was calculated to be most favourable on the (001) surface, followed by the (011) and (111) surfaces [46–48]. The most stable configurations – $(001)_{4F\_S}$, $(011)_{4F\_S,O}$ and $(111)_{fcc\_S}$ – were used to investigate surface coverage, by increasing the number of adsorbed SO_3 molecules ($N_{SO_x}, x = 3$) on each Pt surface, until a monolayer (ML) was obtained. To obtain the lowest energy configurations, shown in Figure 9, various placements of subsequent SO_3 molecules were considered. To determine if adsorption is still favoured as the surface coverage increases, the average adsorption energy (Figure 10(a)) and the sequential adsorption energy Figure 10(b)) as a function of surface coverage were calculated.

As with the adsorption of elemental S and SO on the (001) surface, it can be seen that E_{ads} decreases steadily as the surface coverage increased and is also correlated with the sequential E_{ads} up to $\theta = 0.67$. The initial adsorption configurations up to $\theta = 0.33$ show all the SO_3 in the chosen adsorption mode and site of the isolated molecule. At $\theta = 0.44$, the surface becomes more crowded and one of the SO_3 molecules rotates slightly, but is still bound in the 4F adsorption site, with two O atoms atop a Pt atom. This slight rotation of the SO_3 molecule adsorption also occurs at higher coverages, possibly causing the

smaller adsorption energies. At the highest coverage (θ = 0.78), more distortions can be seen but no reaction occurred between the SO_3 molecules.

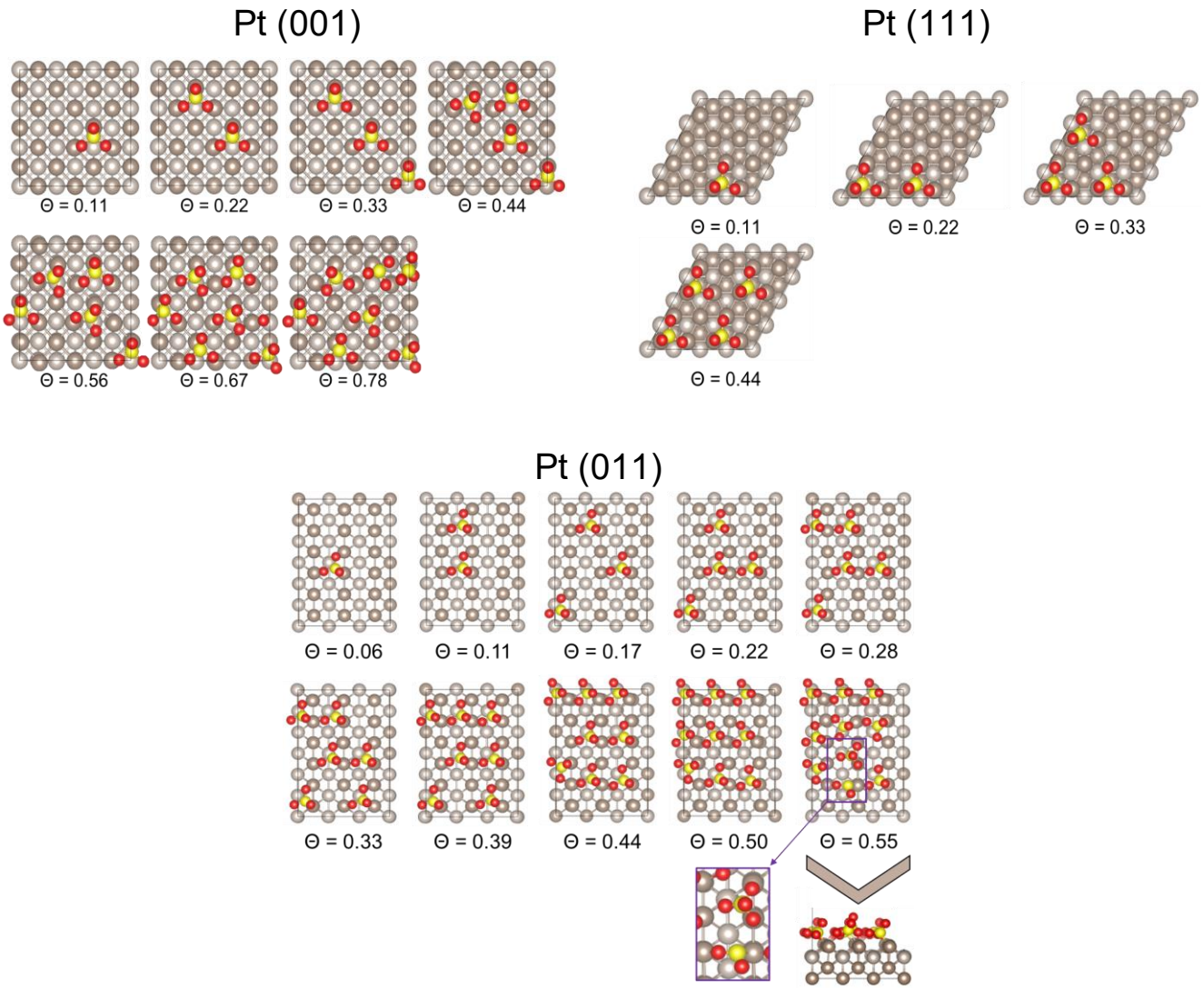

Figure 9 – Increased SO_3 coverage on the Pt (001), (011) and (111) surfaces.

On the Pt (011) surface, E_{ads} again decreases steadily as θ is increased. Furthermore, the sequential E_{ads} also decreases with increased adsorption up to θ = 0.39, but with the addition of another SO_3 (θ = 0.44), the surface becomes more crowded and a slight rotation occurs, causing the sequential E_{ads} to increase. This behaviour was repeated with an additional SO_3 (θ = 0.50), causing all the SO_3 to have the same orientation as with $N_{SO_3} = 1$, thereby increasing the surface strain and resulting in a smaller sequential E_{ads}. The adsorption of an additional SO_3 at θ = 0.55 caused two SO_3 molecules to react and form SO_4 and SO_2. This secondary reaction caused the sequential E_{ads} to increase. No further SO_3

molecules could be adsorbed as a secondary layer started to form, in addition to secondary reactions occurring.

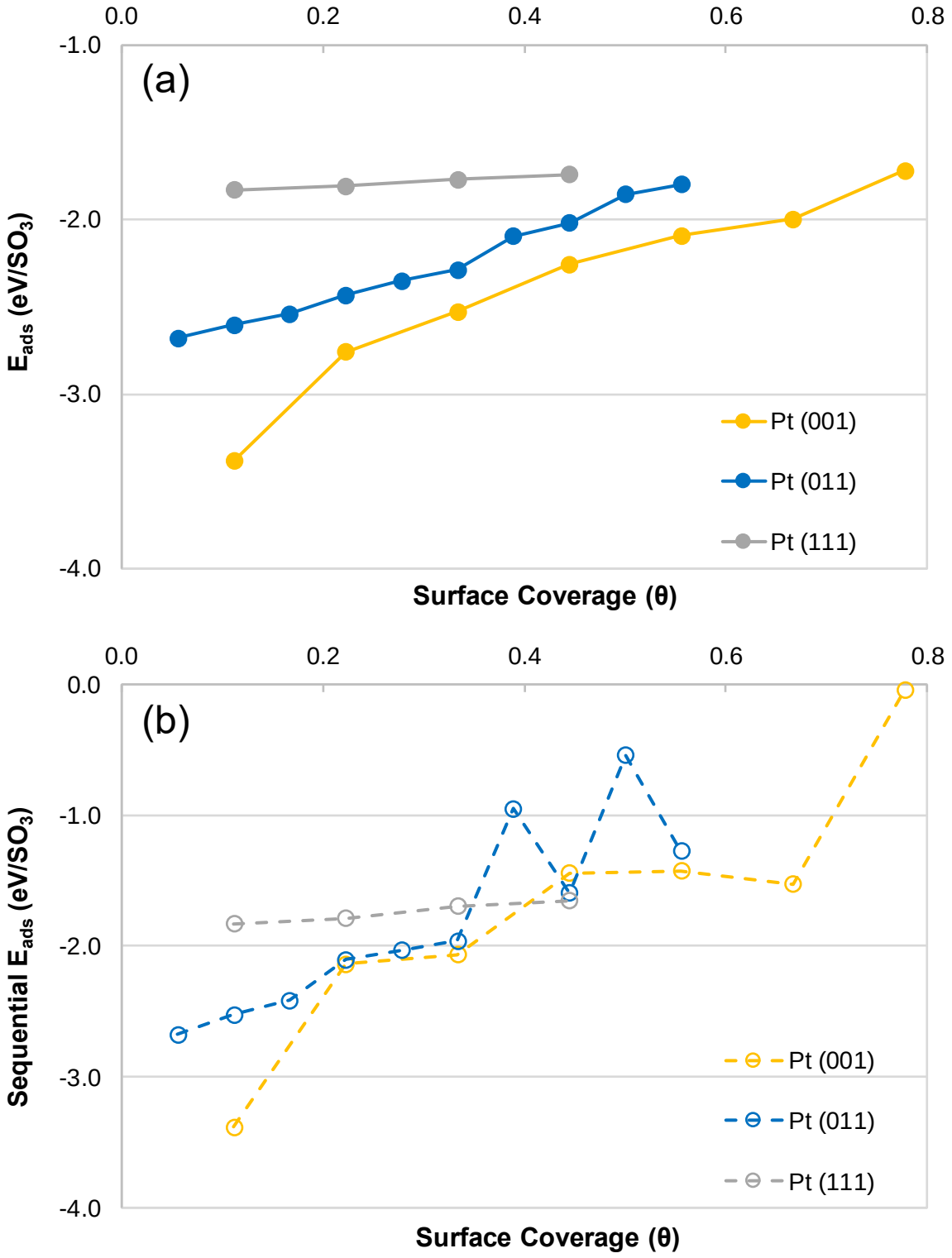

Figure 10 – Average (a) and sequential (b) adsorption energies (E_{ads}) as a function of the SO_3 surface coverage (nm^{-2} Pt) on the Pt (001), (011) and (111) surfaces.

Similar to the increased coverage of SO_3 on the (001) and (011) surfaces, both the E_{ads} and sequential E_{ads} decreased with increased θ. Coverages of θ > 0.44 were not obtained, as this caused not only secondary layers to form, but also the secondary reaction ($2\ SO_3 \rightarrow SO_2 + SO_4$) to occur, as observed on the (011) surface.

When we compare the increased coverages of SO_3 on all three Pt surfaces, we observe that similar to the SO coverages, the highest coverage was achieved on the (001) surface, followed by the (011) and then (111) surfaces. The (011) surface was the most reactive towards secondary reactions between co-adsorbed SO_3 molecules, followed by the (111) surface.

3.5 Thermodynamic Influence on Adsorption

The HyS cycle is operated at 1 atm (1.103 bar) and 350 to 400 K. Phase diagrams have therefore been constructed to determine the effect of temperature and pressure on the surface coverage of S, SO and SO_3. As mentioned, sulphur poisoning may occur on the Pt surface, but we need to establish the effect of temperature and pressure on the surface behaviour. **Error! Reference source not found.** shows the phase diagram for S on the Pt (001), (011) and (111) surfaces. Overall, it can be seen that, compared to pressure, temperature has a bigger effect on the S surface coverage.

The adsorption of S onto the surfaces released energies of between 5 and 7 eV (Table 1). By adding the thermodynamic terms, it can be seen that the Pt surface is very susceptible to sulphur poisoning under experimental conditions, when the surface coverage will be θ > 1. As the temperature increases, subsequent S atoms will react to form S_2 and leave the surface, which is seen at ~700 – 900 K on the (011) surface, although on the (001) and (111) surfaces, S or S_2 only start to leave the surface at T > 1300 K. The temperature was only considered up to 2000 K, as Pt starts melting at 2047 K [84] beyond which it can no longer be considered a stable catalyst. The affinity of S adsorption to any Pt surface, even at very high temperatures, is a clear indication that where possible reactions should be designed to prohibit the formation of S as a by-product.

Figure 12 shows the phase diagram for SO on the Pt (001), (011) and (111) surfaces. The thermodynamic data show that for the adsorption of SO on both the (001) and (011) surfaces, coverages of θ ≥ 1 can be expected. On the (001) surface, the coverage changes from θ = 1.11 to θ = 1.00 between 250 and 400 K and even up to 1000 K, the (001) surface will be fully covered with SO. As such, changes in temperature and pressure cannot be utilised to clear the Pt surface of impurities. On the (011) surface, high coverages are sustained up to 350 and 800 K for the SO_{Bridge} and SO_{4F} configurations, respectively. At higher temperatures, some of the SO molecules will leave the surface without taking part in additional reactions,

but the surface is never entirely free from SO. Interestingly, on the (111) surface, the SO loading is lower, starting at $\theta = 0.89$ and slowly decreasing to $\theta = 0.44$ at $T \geq 550$ K.

The thermodynamic influence on SO_3 adsorption was also only considered up to 1000 K as shown in Figure 13. Similar to the trends with SO, it can be seen in the experimental range (200 -400 K), surface coverage is the highest on the (001) surface ($\theta = 0.66$), followed by the (011) ($0.44 < \theta < 0.56$) and (111) ($\theta = 0.44$) surfaces. Here it can also be seen that temperature has a greater effect on surface coverage, compared to S and SO, possibly due to additional reactions taking place between subsequent SO_3 molecules. Two reactions that may occur include $2\ SO_3 \rightarrow SO$ and SO_4 as was seen on the (011) surface, or $2\ SO_3 \rightarrow 2\ SO_2 + O_2$. The surface can be cleared of SO_3 on both the (111) and (011) surfaces at $T \geq 600$ K and $T \geq 800$ K, respectively.

During the investigation of H_2O and SO_2 adsorption on the Pt surfaces [46–48], temperature played an important role on the surface coverage and that the surface can be cleared of both molecules at elevated temperatures. This is a clear indication that the HyS cycle is temperature sensitive and care should be taken during operation. Elevated temperatures cause firstly the H_2O molecules will desorb from the surface. This in turn could cause an increase in the SO_2 concentration and lead to the formation of more by-products of SO_2, which in turn will impact the efficiency of the HyS cycle.

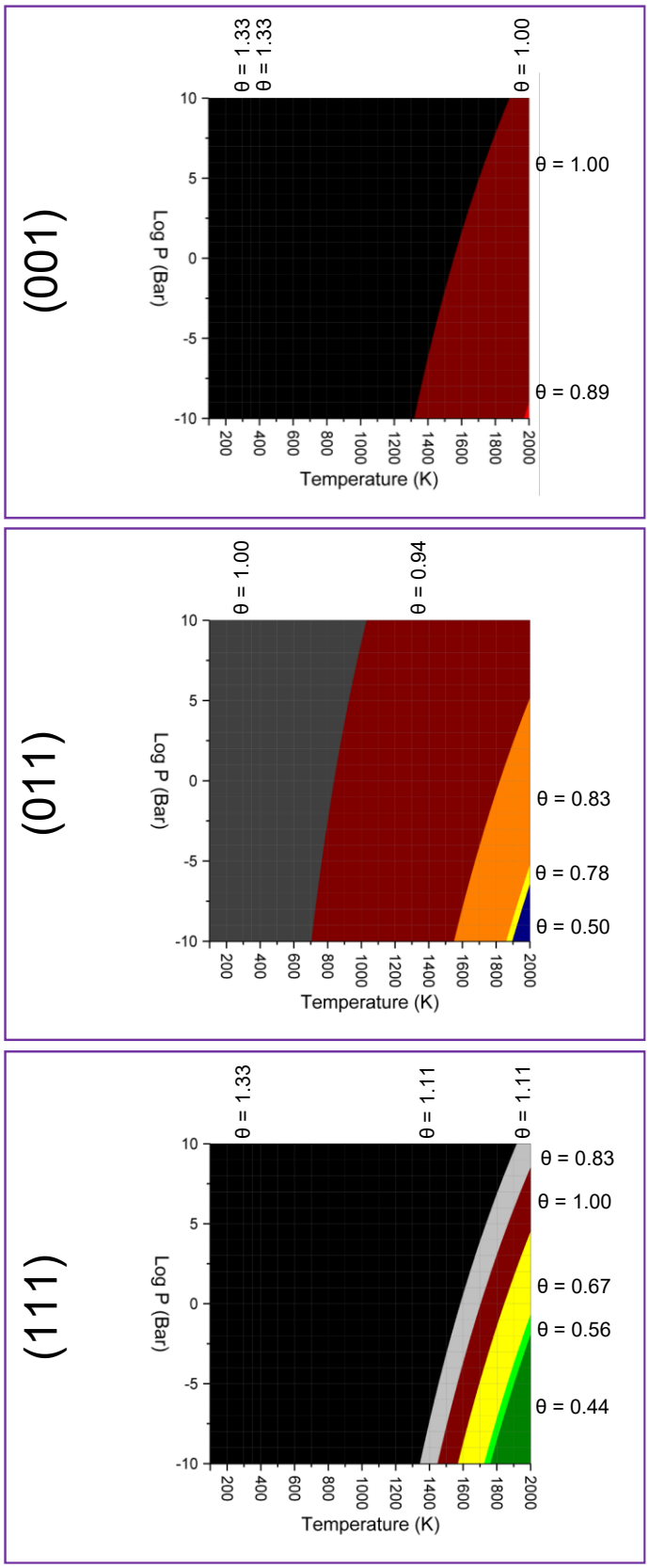

461

462 Figure 11 – Surface phase diagrams in terms of pressure and temperature for the surface coverage of
463 S on the Pt (001), (011) and (111) surfaces. Calculated surface coverage (θ) is given for each colour.

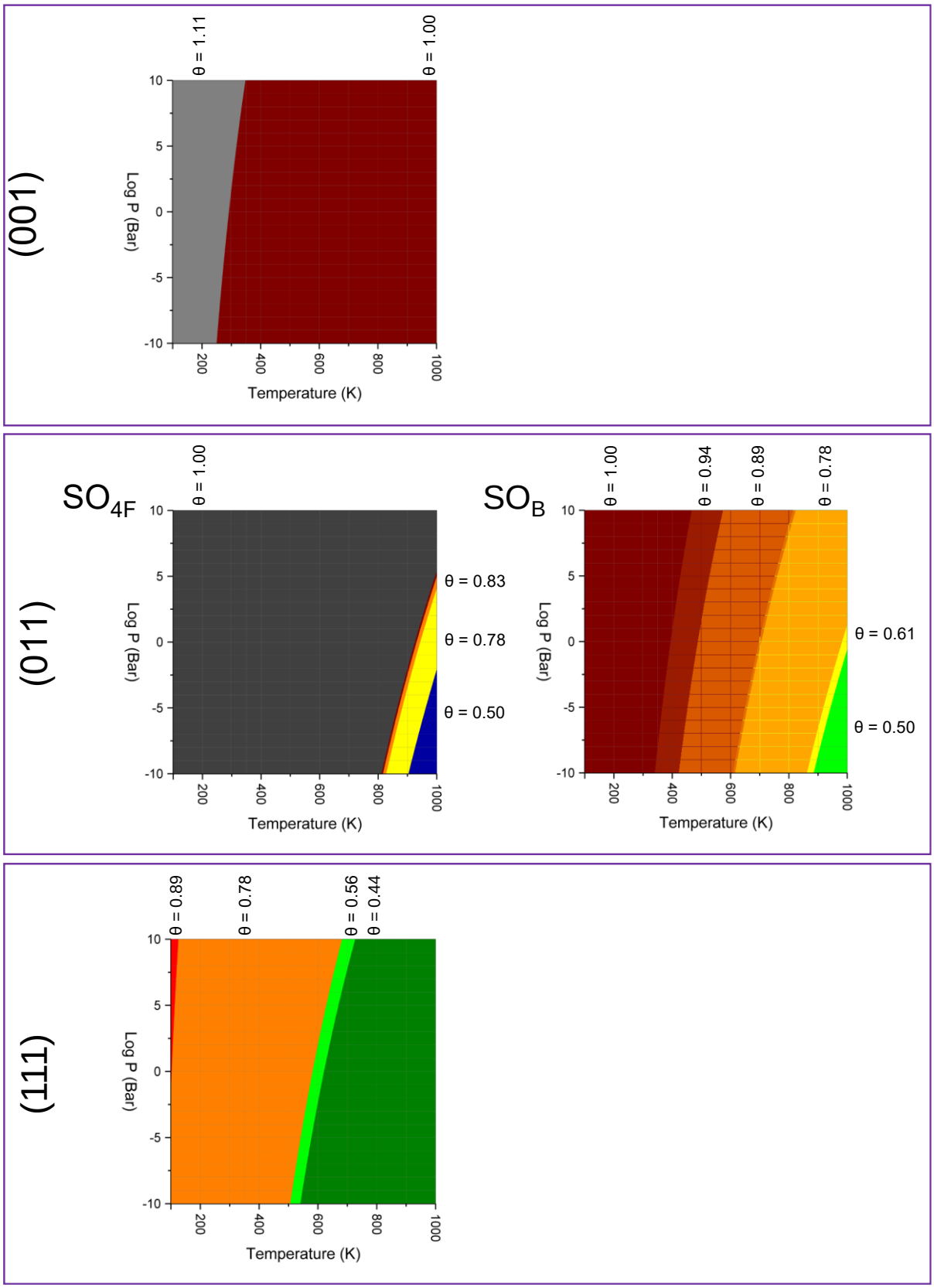

Figure 12 – Surface phase diagrams in terms of pressure and temperature for the surface coverage of SO on the Pt (001), (011) and (111) surfaces. Calculated surface coverage (θ) is given for each colour.

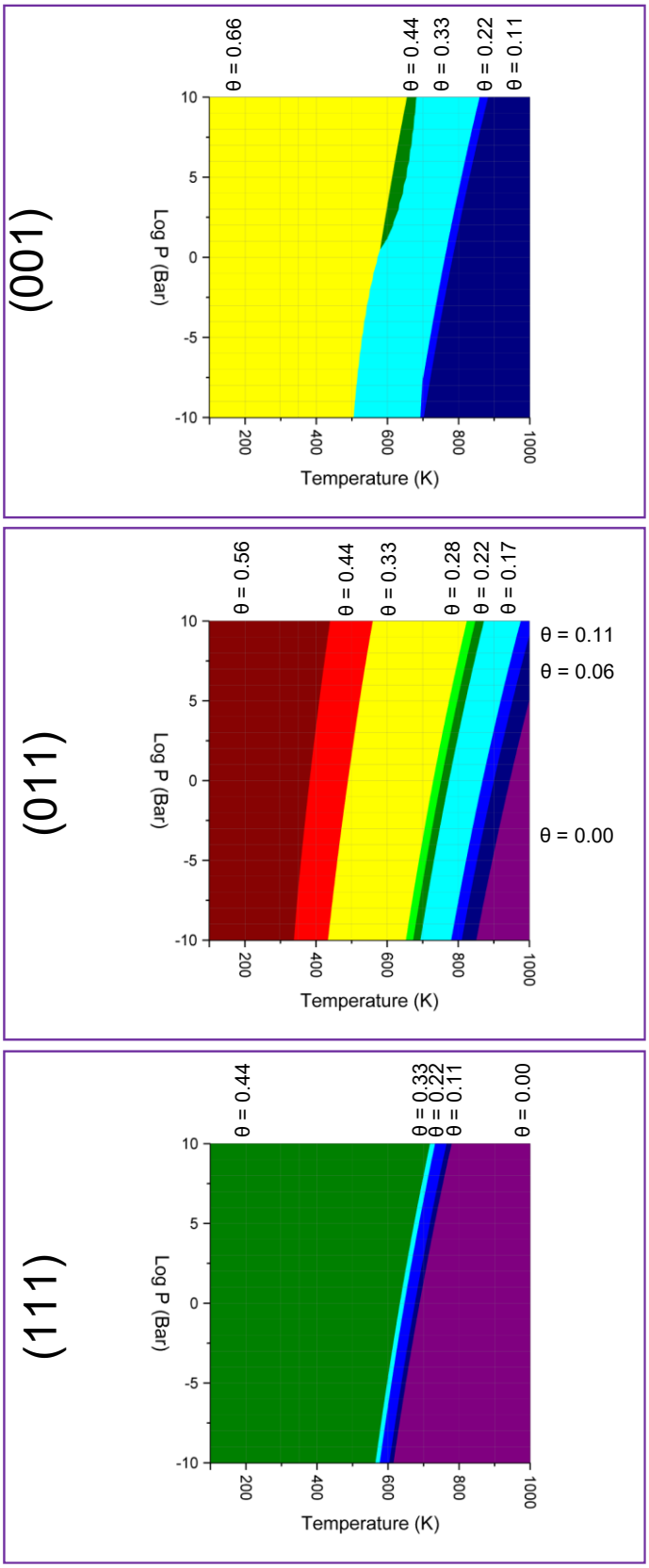

467

468 Figure 13 – Surface phase diagrams in terms of pressure and temperature for the surface coverage of
469 SO_3 on the Pt (001), (011) and (111) surfaces. Calculated surface coverage (θ) is given for each colour.

4. Conclusions

Density functional theory calculations were employed to gain a detailed understanding of the behaviour of S, SO and SO_3 on the Pt (001), (011) and (111) surfaces. Adsorption of all three adsorbates as individual molecules was considered first on all the Pt surfaces. When elemental S was adsorbed, it preferred the 4F hollow site on both the (001) and (011) surfaces (E_{ads_001} = −7.09 eV and E_{ads_011} = −5.47 eV, respectively) and the *fcc* hollow on the (111) surface (E_{ads_111} = −5.47 eV). The adsorption of SO again showed a preference for the 4F hollow on the (001) surface (E_{ads_001} = −5.10 eV), with two possible S,O-adsorptions in the bridge and 4F hollow sites on the (011) surface ($E_{ads\_011\_bridge}$ = −3.56 eV and $E_{ads\_011\_4F}$ = −3.57 eV, respectively) and the *fcc* hollow on the (111) surface (E_{ads_111} = −5.47 eV). Adsorption of SO_3 on the surface was preferred in a S,O,O bound configuration in the 4F (E_{ads_001} = −3.38 eV), 4F (E_{ads_011} = −2.68 eV) and *fcc* (E_{ads_111} = −1.83eV) hollow adsorption sites on the (001), (011) and (111) surfaces, respectively. Overall, it was found that the higher the bond order, the more charge transfer occurs from the Pt surface to the adsorbate. In SO_3 in particular, we noted that the molecule configuration changed from planar to tetrahedral, a clear indication of chemisorption and activation of the molecule.

The surface coverage of all three molecules was increased on all the surfaces, until a monolayer was obtained. The highest surface coverage for S showed the trend $(001)_S = (111)_S > (011)_S$, for SO it was $(001)_{SO} > (011)_{SO} > (111)_{SO}$ and similar for SO_3 $(001)_{SO3} > (011)_{SO3} > (111)_{SO3}$, which indicates that the (001) surface is more susceptible to catalyst poisoning by S species. It was also very evident that both the (001) and (111) surfaces were reactive towards S, leading to the formation of S_2. We found no evidence of secondary reactions of SO on any for the Pt surfaces, but at high coverages of SO_3, we noted the formation of SO_2 and SO_4, especially on the (011) surface.

Thermodynamic effects were also investigated, where we have shown that pressure plays a minimal role in the surface coverage behaviour. An increase in the temperature up to 2000 K showed that the Pt surfaces would still be fully covered with S. The SO coverage showed $\theta \geq 1.00$ on both the (001) and (011) surfaces, and $\theta = 0.78$ on the (111) surface under the experimental temperature and pressure regime, in which the HyS cycle is operated. However, lower coverages of SO_3 were observed and the surface can be cleared at higher temperatures, i.e. $T_{(001)} \geq 1000$ K, $T_{(011)} \geq 800$ K and $T_{(111)} \geq 600$ K.

5. Acknowledgements

We acknowledge the Engineering and Physical Sciences Research Council (EPSRC grants No. EP/K016288/1 and EP/K009567/2) as well as the Economic and Social Research Council (ESRC grant No. ES/N013867/1) and the National Research Foundation of South Africa for funding under the Newton Programme and for a Post-Doctoral Fellowship (NRF grant no. 116728). This research was undertaken

using resources at North-West University, South Africa, and the Supercomputing Facilities at Cardiff University, UK, operated by ARCCA on behalf of Supercomputing Wales (SCW) projects, which is part-funded by the European Regional Development Fund (ERDF) via Welsh Government. We also acknowledge the use of facilities at the Centre for High-Performance Computing (CHPC), South Africa.

6. Data Availability

All data created during this research are openly available from Cardiff University's Research Portal: M.J. Ungerer, C.G.C.E. van Sittert and N.H. de Leeuw (2021). "Behaviour of S, SO and SO_3 on Pt (001), (011) and (111) surfaces: A DFT Study," Cardiff University's Research Portal, V. 1, Dataset. http://doi.org/10.17035/d.2021.0126222709.

7. References

[1] L. Newman, Atmospheric oxidation of sulfur dioxide: A review as viewed from power plant and smelter plume studies, Atmos. Environ. 15 (1981) 2231–2239. https://doi.org/10.1016/0004-6981(81)90255-9.

[2] R.E. Huie, P. Neta, Chemical behavior of sulfur trioxide(1-) (SO3-) and sulfur pentoxide(1-) (SO5-) radicals in aqueous solutions, J. Phys. Chem. 88 (1984) 5665–5669. https://doi.org/10.1021/j150667a042.

[3] Sulfur, in: Chem. Elem., Elsevier, 1997: pp. 645–746. https://doi.org/10.1016/B978-0-7506-3365-9.50021-3.

[4] Z. Klimont, S.J. Smith, J. Cofala, The last decade of global anthropogenic sulfur dioxide: 2000–2011 emissions, Environ. Res. Lett. 8 (2013) 014003. https://doi.org/10.1088/1748-9326/8/1/014003.

[5] W. Aas, A. Mortier, V. Bowersox, R. Cherian, G. Faluvegi, H. Fagerli, J. Hand, Z. Klimont, C. Galy-Lacaux, C.M.B. Lehmann, C.L. Myhre, G. Myhre, D. Olivié, K. Sato, J. Quaas, P.S.P. Rao, M. Schulz, D. Shindell, R.B. Skeie, A. Stein, T. Takemura, S. Tsyro, R. Vet, X. Xu, Global and regional trends of atmospheric sulfur, Sci. Rep. 9 (2019) 953. https://doi.org/10.1038/s41598-018-37304-0.

[6] Rt Hon Michael Gove, Clean Air Strategy Plan, 2019. https://assets.publishing.service.gov.uk/government/uploads/system/uploads/attachment_data/file/770715/clean-air-strategy-2019.pdf.

[7] Q. Zhong, H. Shen, X. Yun, Y. Chen, Y. Ren, H. Xu, G. Shen, W. Du, J. Meng, W. Li, J. Ma, S. Tao, Global Sulfur Dioxide Emissions and the Driving Forces, Environ. Sci. Technol. 54 (2020) 6508–6517. https://doi.org/10.1021/acs.est.9b07696.

[8] G.L. Smith, J.E. Eyley, X. Han, X. Zhang, J. Li, N.M. Jacques, H.G.W. Godfrey, S.P. Argent, L.J. McCormick McPherson, S.J. Teat, Y. Cheng, M.D. Frogley, G. Cinque, S.J. Day, C.C. Tang, T.L. Easun, S. Rudić, A.J. Ramirez-Cuesta, S. Yang, M. Schröder, Reversible coordinative binding and separation of sulfur dioxide in a robust metal–organic framework with open copper sites, Nat. Mater. 18 (2019) 1358–1365. https://doi.org/10.1038/s41563-019-0495-0.

[9] S. Díaz-Abad, M. Millán, M.A. Rodrigo, J. Lobato, Review of Anodic Catalysts for SO2 Depolarized Electrolysis for “Green Hydrogen” Production, Catalysts. 9 (2019) 63. https://doi.org/10.3390/catal9010063.

[10] D.R. Uzun, E. Razkazova-Velkova, V. Beschkov, K. Petrov, A Method for the Simultaneous Cleansing of H 2 S and SO 2, Int. J. Electrochem. 2016 (2016) 1–5. https://doi.org/10.1155/2016/7628761.

[11] C.-C. Cormos, Hydrogen production from fossil fuels with carbon capture and storage based on chemical looping systems, Int. J. Hydrogen Energy. 36 (2011) 5960–5971. https://doi.org/10.1016/j.ijhydene.2011.01.170.

[12] M. Ni, D.Y.C. Leung, M.K.H. Leung, K. Sumathy, An overview of hydrogen production from biomass, Fuel Process. Technol. 87 (2006) 461–472. https://doi.org/10.1016/j.fuproc.2005.11.003.

[13] C. Acar, I. Dincer, G.F. Naterer, Review of photocatalytic water-splitting methods for sustainable hydrogen production, Int. J. Energy Res. 40 (2016) 1449–1473. https://doi.org/10.1002/er.3549.

[14] A. Ursúa, L.M. Gandía, P. Sanchis, Hydrogen Production From Water Electrolysis: Current Status and Future Trends, Proc. IEEE. 100 (2012) 410–426. https://doi.org/10.1109/JPROC.2011.2156750.

[15] F. de Bruijn, The current status of fuel cell technology for mobile and stationary applications, Green Chem. 7 (2005) 132–150. https://doi.org/10.1039/b415317k.

[16] L. Baharudin, M. James Watson, Hydrogen applications and research activities in its production routes through catalytic hydrocarbon conversion, Rev. Chem. Eng. 34 (2017). https://doi.org/10.1515/revce-2016-0040.

[17] L. Schlapbach, A. Züttel, Hydrogen-storage materials for mobile applications, in: Mater. Sustain.

Energy, Co-Published with Macmillan Publishers Ltd, UK, 2010: pp. 265–270. https://doi.org/10.1142/9789814317665_0038.

[18] X. Lin, K.C. Hass, W.F. Schneider, B.L. Trout, Chemistry of Sulfur Oxides on Transition Metals I: Configurations, Energetics, Orbital Analyses, and Surface Coverage Effects of SO 2 on Pt(111), J. Phys. Chem. B. 106 (2002) 12575–12583. https://doi.org/10.1021/jp026128f.

[19] X. Lin, W.F. Schneider, B.L. Trout, Chemistry of sulfur oxides on transition metals. II. Thermodynamics of sulfur oxides on platinum(111), J. Phys. Chem. B. 108 (2004) 250–264. https://doi.org/10.1021/jp035306h.

[20] X. Lin, W.F. Schneider, B.L. Trout, Chemistry of sulfur oxides on transition metals. III. Oxidation of so 2 and self-diffusion of O, SO 2, and SO 3 on Pt(111), J. Phys. Chem. B. 108 (2004) 13329–13340. https://doi.org/10.1021/jp048507.

[21] J.A. O'Brien, J.T. Hinkley, S.W. Donne, S.E. Lindquist, The electrochemical oxidation of aqueous sulfur dioxide: A critical review of work with respect to the hybrid sulfur cycle, Electrochim. Acta. 55 (2010) 573–591. https://doi.org/10.1016/j.electacta.2009.09.067.

[22] M. Polcik, L. Wilde, J. Haase, B. Brena, D. Cocco, G. Comelli, G. Paolucci, Adsorption and temperature-dependent decomposition of SO2 on Cu(100) and Cu(111): A fast and high-resolution core-level spectroscopy study, Phys. Rev. B. 53 (1996) 13720–13724. https://doi.org/10.1103/PhysRevB.53.13720.

[23] M. Polčik, L. Wilde, J. Haase, SO2-induced surface reconstruction of Cu(111): An x-ray-absorption fine-structure study, Phys. Rev. B. 57 (1998) 1868–1874. https://doi.org/10.1103/PhysRevB.57.1868.

[24] M.S. Wilburn, W.S. Epling, SO2 adsorption and desorption characteristics of Pd and Pt catalysts: Precious metal crystallite size dependence, Appl. Catal. A Gen. 534 (2017) 85–93. https://doi.org/10.1016/j.apcata.2017.01.015.

[25] J.A. Rodriguez, J.M. Ricart, A. Clotet, F. Illas, Density functional studies on the adsorption and decomposition of SO2 on Cu(100), J. Chem. Phys. 115 (2001) 454–465. https://doi.org/10.1063/1.1377884.

[26] T. Yokoyama, S. Terada, S. Yagi, A. Imanishi, S. Takenaka, Y. Kitajima, T. Ohta, Surface structures and electronic properties of SO2 adsorbed on Ni(111) and Ni(100) studied by S K-edge X-ray absorption fine structure spectroscopy, Surf. Sci. 324 (1995) 25–34. https://doi.org/10.1016/0039-6028(94)00692-X.

[27] S. Terada, A. Imanishi, T. Yokoyama, S. Takenaka, Y. Kitajima, T. Ohta, Surface structure of SO2 adsorbed on Ni(110) studied by S K-edge X-ray absorption fine structure spectroscopy, Surf. Sci. 336 (1995) 55–62. https://doi.org/10.1016/0039-6028(95)00514-5.

[28] P. Zebisch, M. Weinelt, H.-P. Steinrück, Sulphur dioxide adsorption on the Ni(110) surface, Surf. Sci. 295 (1993) 295–305. https://doi.org/10.1016/0039-6028(93)90276-P.

[29] J. Ahner, A. Effendy, K. Vajen, H.-W. Wassmuth, Chemisorption and multilayer adsorption of SO2 on Ag(111) and Ag(110), Vacuum. 41 (1990) 98–101. https://doi.org/10.1016/0042-207X(90)90285-7.

[30] J.L. Solomon, R.J. Madix, W. Wurth, J. Stohr, NEXAFS and EELS study of the orientation of sulfur dioxide on silver(110), J. Phys. Chem. 95 (1991) 3687–3691. https://doi.org/10.1021/j100162a046.

[31] R.C. Ku, P. Wynblatt, SO2 adsorption on Rh(110) and Pt(110) surfaces, Appl. Surf. Sci. 8 (1981) 250–259. https://doi.org/10.1016/0378-5963(81)90120-3.

[32] J.A. Rodriguez, T. Jirsak, S. Chaturvedi, Reaction of S2 and SO2 with Pd/Rh(111) surfaces: Effects of metal–metal bonding on sulfur poisoning, J. Chem. Phys. 110 (1999) 3138–3147. https://doi.org/10.1063/1.477910.

[33] S. Terada, M. Sakano, Y. Kitajima, T. Yokoyama, T. Ohta, Adsorption of SO2 on Pd(100) Studied by S K-Edge XAFS, Le J. Phys. IV. 7 (1997) C2-703-C2-704. https://doi.org/10.1051/jp4:1997211.

[34] M.L. Burke, R.J. Madix, Hydrogen on Pd(100)-S: the effect of sulfur on precursor mediated adsorption and desorption, Surf. Sci. 237 (1990) 1–19. https://doi.org/10.1016/0039-6028(90)90515-A.

[35] J.M. Saleh, Interaction of sulphur compounds with palladium, Trans. Faraday Soc. 66 (1970) 242. https://doi.org/10.1039/tf9706600242.

[36] M.L. Burke, R.J. Madix, SO2 structure and reactivity on clean and sulfur modified Pd(100), Surf. Sci. 194 (1988) 223–244. https://doi.org/10.1016/0039-6028(94)91257-2.

[37] S. Astegger, E. Bechtold, Adsorption of sulfur dioxide and the interaction of coadsorbed oxygen and sulfur on Pt(111), Surf. Sci. 122 (1982) 491–504. https://doi.org/10.1016/0039-6028(82)90098-X.

[38] U. Köhler, H.-W. Wassmuth, SO2 adsorption and desorption kinetics on Pt(111), Surf. Sci. 126 (1983) 448–454. https://doi.org/10.1016/0039-6028(83)90742-2.

[39] Y.-M. Sun, D. Sloan, D.J. Alberas, M. Kovar, Z.-J. Sun, J.M. White, SO2 adsorption on Pt(111):

HREELS, XPS and UPS study, Surf. Sci. 319 (1994) 34–44. https://doi.org/10.1016/0039-6028(94)90567-3.

[40] M. Polčik, L. Wilde, J. Haase, B. Brena, G. Comelli, G. Paolucci, High-resolution XPS and NEXAFS study of SO2 adsorption on Pt(111): two surface SO2 species, Surf. Sci. 381 (1997) L568–L572. https://doi.org/10.1016/S0039-6028(97)00060-5.

[41] H.R. Colón-Mercado, D.T. Hobbs, Catalyst evaluation for a sulfur dioxide-depolarized electrolyzer, Electrochem. Commun. 9 (2007) 2649–2653. https://doi.org/10.1016/j.elecom.2007.08.015.

[42] P.W.T. Lu, R.L. Ammon, An Investigation of Electrode Materials for the Anodic Oxidation of Sulfur Dioxide in Concentrated Sulfuric Acid, J. Electrochem. Soc. 127 (1980) 2610. https://doi.org/10.1149/1.2129530.

[43] A.J. Appleby, B. Pinchon, Electrochemical aspects of the H2SO4SO2 thermoelectrochemical cycle for hydrogen production, Int. J. Hydrogen Energy. 5 (1980) 253–267. https://doi.org/10.1016/0360-3199(80)90070-1.

[44] B. Meyer, Elemental sulfur, Chem. Rev. 76 (1976) 367–388. https://doi.org/10.1021/cr60301a003.

[45] B.D. Struck, R. Junginger, D. Boltersdorf, J. Gehrmann, The anodic oxidation of sulfur dioxide in the sulfuric acid hybrid cycle, Int. J. Hydrogen Energy. 5 (1980) 487–497. https://doi.org/10.1016/0360-3199(80)90055-5.

[46] M.J. Ungerer, D. Santos-Carballal, A. Cadi-Essadek, C.G.C.E. van Sittert, N.H. de Leeuw, Interaction of H2O with the Platinum Pt (001), (011) and (111) Surfaces: A Density Functional Theory Study with Long-Range Dispersion Corrections, J. Phys. Chem. C. (2019) acs.jpcc.9b06136. https://doi.org/10.1021/acs.jpcc.9b06136.

[47] M.J. Ungerer, D. Santos-Carballal, A. Cadi-Essadek, C.G.C.E. Van Sittert, N.H. de Leeuw, Interaction of SO2 with the Platinum (001), (011) and (111) Surfaces: A DFT Study, Surf. Chem. Catal. (2020). https://www.mdpi.com/journal/catalysts/special_issues/surf_catal.

[48] M.J. Ungerer, D. Santos-Carballal, C.G.C.E. van Sittert, N.H. De Leeuw, Competitive Adsorption of H2O and SO2 on Catalytic Platinum Surfaces: a Density Functional Theory Study, South African Chem. Inst. SPECIAL ED (2020). https://doi.org/10.17159/0379-4350/2020/v74a00.

[49] G. Kresse, J. Hafner, Ab initio molecular dynamics for liquid metals, Phys. Rev. B. 47 (1993) 558–561. https://doi.org/10.1103/PhysRevB.47.558.

[50] G. Kresse, J. Hafner, Ab initio molecular-dynamics simulation of the liquid-metalamorphous-semiconductor transition in germanium, Phys. Rev. B. 49 (1994) 14251–14269.

https://doi.org/10.1103/PhysRevB.49.14251.

[51] G. Kresse, J. Furthmüller, Efficient iterative schemes for ab initio total-energy calculations using a plane-wave basis set, Phys. Rev. B. 54 (1996) 11169–11186. https://doi.org/10.1103/PhysRevB.54.11169.

[52] G. Kresse, J. Furthmüller, Efficiency of ab-initio total energy calculations for metals and semiconductors using a plane-wave basis set, Comput. Mater. Sci. 6 (1996) 15–50. https://doi.org/10.1016/0927-0256(96)00008-0.

[53] P.E. Blöchl, Projector augmented-wave method, Phys. Rev. B. 50 (1994) 17953–17979. https://doi.org/10.1103/PhysRevB.50.17953.

[54] G. Kresse, D. Joubert, From ultrasoft pseudopotentials to the projector augmented-wave method, Phys. Rev. B. 59 (1999) 1758–1775. https://doi.org/10.1103/PhysRevB.59.1758.

[55] J.P. Perdew, K. Burke, M. Ernzerhof, Generalized Gradient Approximation Made Simple, Phys. Rev. Lett. 77 (1996) 3865–3868. https://doi.org/10.1103/PhysRevLett.77.3865.

[56] S. Grimme, S. Ehrlich, L. Goerigk, Effect of the damping function in dispersion corrected density functional theory, J. Comput. Chem. 32 (2011) 1456–1465. https://doi.org/10.1002/jcc.21759.

[57] S. Posada-Pérez, D. Santos-Carballal, U. Terranova, A. Roldan, F. Illas, N.H. de Leeuw, CO2 interaction with violarite (FeNi2S4) surfaces: a dispersion-corrected DFT study, Phys. Chem. Chem. Phys. 20 (2018) 20439–20446. https://doi.org/10.1039/C8CP03430C.

[58] S.S. Tafreshi, A. Roldan, N.Y. Dzade, N.H. de Leeuw, Adsorption of hydrazine on the perfect and defective copper (111) surface: A dispersion-corrected DFT study, Surf. Sci. 622 (2014) 1–8. https://doi.org/10.1016/j.susc.2013.11.013.

[59] N.Y. Dzade, A. Roldan, N.H. de Leeuw, Activation and dissociation of CO 2 on the (001), (011), and (111) surfaces of mackinawite (FeS): A dispersion-corrected DFT study, J. Chem. Phys. 143 (2015) 094703. https://doi.org/10.1063/1.4929470.

[60] A.K. Mishra, A. Roldan, N.H. de Leeuw, CuO Surfaces and CO2 Activation: A Dispersion-Corrected DFT+ U Study, J. Phys. Chem. C. 120 (2016) 2198–2214. https://doi.org/10.1021/acs.jpcc.5b10431.

[61] S. Grimme, J. Antony, S. Ehrlich, H. Krieg, A consistent and accurate ab initio parametrization of density functional dispersion correction (DFT-D) for the 94 elements H-Pu, J. Chem. Phys. 132 (2010) 154104. https://doi.org/10.1063/1.3382344.

687 [62] M. Methfessel, A.T. Paxton, High-precision sampling for Brillouin-zone integration in metals, Phys.
688 Rev. B. 40 (1989) 3616–3621. https://doi.org/10.1103/PhysRevB.40.3616.

689 [63] P.E. Blöchl, O. Jepsen, O.K. Andersen, Improved tetrahedron method for Brillouin-zone
690 integrations, Phys. Rev. B. 49 (1994) 16223–16233. https://doi.org/10.1103/PhysRevB.49.16223.

691 [64] G. Corbel, M. Topić, A. Gibaud, C.I. Lang, Selective dry oxidation of the ordered Pt-11.1 at.% v
692 alloy surface evidenced by in situ temperature-controlled X-ray diffraction, J. Alloys Compd. 509
693 (2011) 6532–6538. https://doi.org/10.1016/j.jallcom.2011.03.079.

694 [65] H.J. Monkhorst, J.D. Pack, Special points for Brillouin-zon integrations, Phys. Rev. B. 13 (1976)
695 5188–5192. https://doi.org/10.1103/PhysRevB.16.1748.

696 [66] J.W. Arblaster, Crystallographic properties of platinum, Platin. Met. Rev. 41 (1997) 12–21.
697 https://doi.org/http://www.technology.matthey.com/article/41/1/12-21/.

698 [67] J.W. Arblaster, Crystallographic properties of platinum (Errata), Platin. Met. Rev. 50 (2006) 118–
699 119. https://doi.org/10.1595/147106706X129088.

700 [68] G.W. Watson, E.T. Kelsey, N.H. de Leeuw, D.J. Harris, S.C. Parker, Atomistic simulation of
701 dislocations, surfaces and interfaces in MgO, J. Chem. Soc. Faraday Trans. 92 (1996) 433.
702 https://doi.org/10.1039/ft9969200433.

703 [69] G. Henkelman, A. Arnaldsson, H. Jónsson, A fast and robust algorithm for Bader decomposition
704 of charge density, Comput. Mater. Sci. 36 (2006) 354–360.
705 https://doi.org/10.1016/j.commatsci.2005.04.010.

706 [70] E. Sanville, S.D. Kenny, R. Smith, G. Henkelman, Improved grid-based algorithm for Bader charge
707 allocation, J. Comput. Chem. 28 (2007) 899–908. https://doi.org/10.1002/jcc.20575.

708 [71] W. Tang, E. Sanville, G. Henkelman, A grid-based Bader analysis algorithm without lattice bias.,
709 J. Phys. Condens. Matter. 21 (2009) 084204. https://doi.org/10.1088/0953-8984/21/8/084204.

710 [72] M. Yu, D.R. Trinkle, Accurate and efficient algorithm for Bader charge integration, J. Chem. Phys.
711 134 (2011) 1–8. https://doi.org/10.1063/1.3553716.

712 [73] S.S. Tafreshi, A. Roldan, N.H. de Leeuw, Hydrazine network on Cu(111) surface: A Density
713 Functional Theory approach, Surf. Sci. 637–638 (2015) 140–148.
714 https://doi.org/10.1016/j.susc.2015.04.001.

715 [74] D. Santos-Carballal, A. Roldan, R. Grau-Crespo, N.H. de Leeuw, A DFT study of the structures,
716 stabilities and redox behaviour of the major surfaces of magnetite Fe3O4, Phys. Chem. Chem.

Phys. 16 (2014) 21082–21097. https://doi.org/10.1039/C4CP00529E.

[75] M. Chase, NIST-JANAF Thermochemical Tables, 4th Edition, 1998. https://doi.org/citeulike-article-id:12140840.

[76] J.-H. Wang, M. Liu, Computational study of sulfur–nickel interactions: A new S–Ni phase diagram, Electrochem. Commun. 9 (2007) 2212–2217. https://doi.org/10.1016/j.elecom.2007.06.022.

[77] W.R. Tyson, W.A. Miller, Surface free energies of solid metals: Estimation from liquid surface tension measurements, Surf. Sci. 62 (1977) 267–276. https://doi.org/10.1016/0039-6028(77)90442-3.

[78] Z. Jian-Min, M. Fei, X. Ke-Wei, Calculation of the surface energy of fcc metals with modified embedded-atom method, Chinese Phys. 13 (2004) 1082–1090. https://doi.org/10.1088/1009-1963/13/7/020.

[79] D.R. Alfonso, Computational Studies of Experimentally Observed Structures of Sulfur on Metal Surfaces, J. Phys. Chem. C. 115 (2011) 17077–17091. https://doi.org/10.1021/jp2048426.

[80] C.R. Bernard Rodríguez, J.A. Santana, Adsorption and diffusion of sulfur on the (111), (100), (110), and (211) surfaces of FCC metals: Density functional theory calculations, J. Chem. Phys. 149 (2018) 204701. https://doi.org/10.1063/1.5063464.

[81] B.A. Lindquist, T.H. Dunning, The nature of the SO bond of chlorinated sulfur–oxygen compounds, Theor. Chem. Acc. 133 (2014) 1443. https://doi.org/10.1007/s00214-013-1443-8.

[82] R.J. Gillespie, E.A. Robinson, the Sulphur–Oxygen Bond in Sulphuryl and Thionyl Compounds: Correlation of Stretching Frequencies and Force Constants With Bond Lengths, Bond Angles, and Bond Orders, Can. J. Chem. 41 (1963) 2074–2085. https://doi.org/10.1139/v63-299.

[83] G. Dai, X. Wang, H. You, Y. Wang, Z. Shan, H. Tan, Catalytic function of ferric oxide and effect of water on the formation of sulfur trioxide, J. Environ. Manage. 264 (2020) 110499. https://doi.org/10.1016/j.jenvman.2020.110499.

[84] G.A. Slack, Platinum as a Thermal Conductivity Standard, J. Appl. Phys. 35 (1964) 339–344. https://doi.org/10.1063/1.1713313.